Precision Measurements of Higgs Hadronic Decay Modes at the FCC-ee

Andrea Del Vecchio, a Jan Eysermans, f Loukas Gouskos, d George Iakovidis, c Alexis Maloizel, e Giovanni Marchiori, e and Michele Selvaggi b

```
<sup>a</sup>La Sapienza, Roma, Italy
```

E-mail: andrea.del.vecchio@cern.ch, jan.eysermans@cern.ch, loukas.gouskos@cern.ch, george.iakovidis@cern.ch, alexis.maloizel@ens-paris-saclay.fr, giovanni.marchiori@cern.ch, michele.selvaggi@cern.ch

ABSTRACT: The expected precision at the FCC-ee on the product $\sigma \times \mathcal{B}(H \to b\bar{b}, c\bar{c}, s\bar{s}, gg)$ of Higgs boson production cross sections times branching ratios of hadronic decays is presented. This study provides the first comprehensive determination of all major hadronic Higgs decay modes in a combined fit at future e^+e^- colliders, using both Higgs-strahlung (ZH) and Vector boson fusion $(\nu\bar{\nu}H)$ production processes, with a full treatment of interference effects in the $\nu\bar{\nu}jj$ final state. It assumes four identical IDEA detectors collecting e^+e^- collisions at $\sqrt{s}=240$ and 365 GeV. The combination of all channels across both energies, with full covariance between production and decay modes, yields a production cross-section times branching-ratio precision at the percent to per-mil level for the dominant hadronic final states $(b\bar{b}, c\bar{c}, gg)$. These results provide a comprehensive input to the determination of Higgs coupling projections at the FCC-ee, and they establish for the first time sensitivity to the rare decay $H \to s\bar{s}$, demonstrating that FCC-ee has the potential to provide evidence of the strange-quark Yukawa coupling.

^bEuropean Organisation for Nuclear Research (CERN), Geneva, Switzerland

^cBrookhaven National Laboratory, Upton, NY, USA

^dBrown University, Providence, RI, USA

^eLaboratoire AstroParticule et Cosmologie, (CNRS/IN2P3), Paris, France

^f Massachusetts Institute of Technology, Boston, USA

Co	ontents	
1	Introduction	1
2	The detector concept	3
3	Event simulation	4
4	Detector response and global event reconstruction	5
5	The $\ell\ell jj$ final state	6
	5.1 Event selection	6
	5.2 Event classification	7
6	The $ uar{ u}jj$ final state	10
	6.1 Event selection	10
	6.2 Event classification	11
7	The $jjjj$ final state	12
	7.1 Event selection	13
	7.2 Event classification	16
8	Signal strength measurement	17
9	Conclusion	21
\mathbf{A}	Appendix	21

1 Introduction

The discovery of a Higgs boson (H) with mass $m_H \simeq 125\,\mathrm{GeV}$ by the ATLAS and CMS experiments [1, 2] was a landmark achievement in the understanding of the electroweak (EW) symmetry breaking [1, 2]. All measurements so far [3–13] (i.e., interactions with gauge bosons, third generation fermions, as well as rare decays to $Z\gamma$ and to a pair of muons) show that its properties are consistent with those of the standard model (SM) Higgs boson [14, 15].

Precise measurements of the Higgs boson hadronic branching fractions are essential to test the mechanism of fermion mass generation in the SM. They provide direct access to the tree-level Yukawa couplings of the Higgs boson to bottom, charm, and strange quarks. In the SM, Yukawa couplings are proportional to the corresponding quark masses, and verifying this scaling is a fundamental test of the Higgs mechanism. A wide range of

extensions of the SM predict possible deviations from this linear relation. Models such as Minimal Flavour Violation (MFV), strongly interacting or composite Higgs models, two Higgs doublet models (2HDM), supersymmetric extensions of the SM, and models with vector-like quarks can induce modifications of the tree level Yukawa couplings. A discussion of these models and their phenomenological implications can be found e.g. in Refs. [16, 17].

The first and second generations are especially informative: they directly test the mass–proportionality pattern far from the heavy-flavour regime and are uniquely sensitive to flavour-specific new dynamics. However, even at the High-Luminosity LHC (HL-LHC), most Higgs couplings are projected to reach at best few-percent precision, and direct probes of second-generation quark Yukawas remain challenging; under optimistic assumptions, only an evidence-level sensitivity ($\sim 3\sigma$) to $H \rightarrow c\bar{c}$ is anticipated [16, 18]. Moreover, these measurements rely on the assumption that the production cross-sections are equal to their SM-predicted values, thus introducing a degree of model dependence in the results.

In the SM, the hadronic branching ratios (\mathcal{B}) sum to about 69.32%. $\mathcal{B}(H \to s\bar{s})$ is expected to be around 2.4×10^{-4} , assuming $\bar{m}_s(2 \text{ GeV}) = 93 \text{ MeV}$ [19]. Therefore, precise measurements of the Higgs hadronic branching fractions are essential to test the mechanism of fermion mass generation in the SM. They give direct access to the tree-level Yukawa couplings to bottom, charm, and strange quarks, and constrain the effective, loop-induced coupling to gluons, which can be sensitive to new heavy coloured states.

The FCC-ee [20, 21], a high-luminosity circular e^+e^- collider, is expected to produce large Higgs samples in a clean environment at centre-of-mass energies around 240 GeV and above. At these energies, Higgs production is dominated by Higgs-strahlung ($e^+e^- \to ZH$), with cross-sections $\sigma_{ZH} \simeq 200$ fb at $\sqrt{s} = 240$ GeV and $\sigma_{ZH} \approx 125$ fb at $\sqrt{s} = 365$ GeV. The Vector-boson fusion (VBF) process also contributes at smaller rates: 0.4 (3.2) fb for $ZZ \to e^+e^-H$ and 6.1 (29.2) fb for $WW \to \nu_e\bar{\nu}_eH$ at $\sqrt{s} = 240$ (365) GeV. With $\mathcal{L} = 10.8$ ab⁻¹ at 240 GeV collected over three years with four detectors, about 2.2×10^6 Higgs-strahlung and 6.5×10^4 VBF events are expected. An additional five years at 365 GeV would yield about 370k (92k) Higgs decays from ZH (VBF) for ~ 3.12 ab⁻¹.

At the FCC-ee, the absence of pile-up and underlying event, and backgrounds dominated by EW processes, lead to much larger signal-to-background ratios than at the LHC, especially for hadronic decays. A further advantage is the recoil-mass technique, which measures the total Higgs production cross-section independently of the Higgs decay. Reconstructing each decay mode then enables direct branching-ratio measurements; a joint analysis of these results yields in a model-independent way, the total Higgs width and its couplings.

Previous studies at other e^+e^- Higgs factories indicate sub-percent to few-percent precision on the leading hadronic modes. At the proposed Linear Collider Facilities (LCF), with 2.7 ab⁻¹ at $\sqrt{s} = 250 \,\text{GeV}$, the projected statistical uncertainties on $\sigma_{ZH} \times \mathcal{B}(H \to b\bar{b}, c\bar{c}, gg)$ are about 0.41%, 2.5%, and 2.1%, respectively [22]. At the proposed CEPC, projections with 20 ab⁻¹ at $\sqrt{s} = 240 \,\text{GeV}$ yield approximately 0.14%, 2.02%, and 0.81% for the same quantities.

This article studies the sensitivity to $\sigma \times \mathcal{B}(H \to b\bar{b}, c\bar{c}, s\bar{s}, gg)$ at the FCC-ee, assuming

four detectors with performance identical to those expected for the IDEA concept [23], and integrated luminosities of 10.8 (3.12) ab⁻¹ at $\sqrt{s} = 240$ (365) GeV. The primary production mode is ZH with the Z decaying to e^+e^- , $\mu^+\mu^-$, $\nu\bar{\nu}$, or quark–antiquark pairs of any flavour except $t\bar{t}$. The VBF production mode also contributes when the Z is reconstructed as e^+e^- (via ZZ fusion) or as $\nu\bar{\nu}$ (via WW fusion); the latter shares a final state with $Z(\nu\bar{\nu})H$ and is treated within the same analysis. The Z-fusion contribution is neglected due to its small rate except, in the $\ell\ell jj$ channel at $\sqrt{s}=365\,\mathrm{GeV}$ where it accounts for about 27% of the total and is folded into the SM yields¹. The $\ell\ell jj$ analysis is nevertheless optimised for ZH.

This work provides a coherent determination of all major hadronic Higgs decay modes in a single combined fit at the FCC-ee, simultaneously accounting for both ZH and VBF production and including a full treatment of interference effects in the $\nu\bar{\nu}jj$ final state. Measurements at $\sqrt{s}=240$ and 365 GeV are combined, yielding the expected precision on $\sigma \times \mathcal{B}$ for $H \to b\bar{b}$, $c\bar{c}$, $s\bar{s}$, and gg at both energies. Together with the FCC-ee determination of the total Higgs production cross-section [24], these results provide essential input to model-independent global Higgs-coupling fits and to the extraction of the total Higgs width, expected to reach 0.78% precision at the FCC-ee [21]. For the first time, the rare decay $H \to s\bar{s}$ is included consistently within the same combined fit, indicating a potential sensitivity to the strange-quark Yukawa coupling. The results have been provided to the European Strategy for Particle Physics Update (ESPPU2026) [25] and to the Physics Briefing Book [26].

The article is organised as follows. Section 2 summarises briefly the main features of the IDEA detector concept. The progress on the particle detection techniques that will allow building next-generation devices that can perform efficient tagging of jets produced by the hadronisation of gluons, charm quarks and strange quarks is discussed. The simulated signal and background event samples used for this study are described in Section 3. Section 4 illustrates how particle candidates and events are reconstructed. The following three sections describe the event selection and categorisation of the three final states under study, respectively $\ell\ell jj$, $\nu\bar{\nu}jj$, and jjjj. The measurement of $\sigma \times \mathcal{B}$ from the yields and distribution of discriminant variables in the reconstructed event categories for each of the three analyses and their joint interpretation is discussed in Section 8.

2 The detector concept

The results presented in this study are based on the projected performance of the IDEA detector concept [27]. The detector, roughly 11×11 m in height and length respectively, consists of nested sub-detectors arranged around an FCC-ee interaction point.

The tracking system includes a silicon pixel vertex detector, surrounded by a low-mass drift chamber and an outer silicon wrapper. The vertex detector (VXD) includes a cylindrical barrel of five single layers at radii between R = 1.2 and 31.5 cm, and two endcaps (one per side of the IP), each made of three single-layer silicon disks. The VXD is

¹At $\sqrt{s} = 240 \,\text{GeV}$ the Z-fusion yield is about 3%.

designed to be ultra-light to minimise multiple scattering, and features an excellent single-point resolution of $\sigma=3\,\mu\mathrm{m}$, with the innermost layer positioned at a radius of 1.37 cm and the beam pipe at 1.0 cm. The resulting excellent impact-parameter resolution allows for efficient and pure identification of charm and bottom jets against those originating from gluons and light flavor jets. The drift chamber (DC) has a total length of about 4 m and 112 wire layers at radii between 35 and 200 cm, enabling continuous tracking and particle identification. The DC material traversed at 90° is $\sim 1.6\%\,X_0$. The silicon wrapper surrounds the DC, and provides a precise spatial point at the end of the trajectory and measuring the charged-particle time of arrival. The combined particle-identification capabilities of the drift chamber and silicon wrapper timing allow for $3\sigma\,K/\pi$ separation up to momenta of about 30 GeV. Such particle identification performance is fundamental for tagging kaons within heavy-flavour jets, and in particular for identifying leading high momentum kaons that provide a distinctive signature of strange quark jets. The tracker operates in a uniform 2 T axial magnetic field, provided by a thin superconducting solenoid covering radii between about 2.1 and 2.4 m.

Outside the tracker, a preshower based on lead and Micro-Pattern Gas Detectors (MPGDs), followed by electromagnetic and hadronic calorimeters, measures shower positions and energies and thus enables the reconstruction of photons, electrons, and charged and neutral hadrons. Downstream of the preshower, a Dual-Readout calorimeter (DRC) of about 2 m depth (corresponding to 7 interaction lengths), made of lead–fibre technology, measures electromagnetic and hadron showers. The simulations used here also include a 20 cm-deep crystal electromagnetic calorimeter (ECAL) added upstream of the DRC, with a thin solenoid placed between the ECAL and DRC to preserve the excellent electromagnetic energy resolution. The DRC features a stochastic term of $30\%/\sqrt{E}$ for hadrons, which translates into an excellent visible energy and jet energy resolution, a critical aspect for the reconstruction of resonant Higgs hadronic decay modes. Finally, layers of μ -RWELL chambers embedded in the magnet return yoke surround the calorimeters and provide an efficient, cost-effective solution for identifying penetrating muons.

3 Event simulation

Signal samples were generated with WHIZARD [28], interfaced to PYTHIA 6 [29] for Higgs boson decays and parton showering. Non-Higgs backgrounds were generated with WHIZARD for processes producing purely leptonic final states, and for W-fusion $\nu_e \bar{\nu}_e Z$ production. PYTHIA 8 [30] was used for processes producing hadrons in the final state.

Events were generated at both e^+e^- centre-of-mass energies of 240 GeV and 365 GeV. All samples are normalised to the expected integrated luminosities of 10.8 (3.12) ab⁻¹ at $\sqrt{s} = 240$ (365) GeV, using the highest available order theoretical predictions for their production cross-sections and branching ratios.

A Gaussian smearing of the beam particle energy is applied to simulate the momentum spread of the particles in the beam bunches. The collision crossing angle is not taken into account in the simulation. The nominal IP corresponds to the nominal centre of the detector, which is also the origin of the detector coordinate system. A right-handed

coordinate system is used, with its origin at the nominal interaction point in the centre of the detector and the z-axis along the beam pipe. The x-axis points from the IP to the centre of the ring, and the y-axis points upwards. Cylindrical coordinates (r, ϕ) are used in the transverse plane. The beamspot has an energy dependent longitudinal spread of $\sim 1 \,\mathrm{mm}$ and transverse sizes of $\sim 10 \,\mathrm{\mu m}$ (x) and $\sim 30 \,\mathrm{nm}$ (y).

WHIZARD was used for the production of Higgs boson event samples, with the Higgs boson decaying to $b\bar{b}$, $c\bar{c}$, gg, $s\bar{s}$ or the other dominant final states ($\tau\tau$, WW, ZZ). WHIZARD generates the kinematic distributions of the Higgs boson and of the accompanying leptons, while the Higgs boson decay and parton showering are handled by PYTHIA 6 [29]. Both Higgs-strahlung and vector-boson-fusion production modes were included at $\sqrt{s}=240$ and 365 GeV. Dedicated samples of Higgs boson decays to $b\bar{b}$, $c\bar{c}$, $s\bar{s}$, and gg were also produced for training and validating the jet-tagging algorithms. These were generated independently of the analysis samples to avoid statistical correlations. WHIZARD was also used for the production of non-Higgs background samples such as $ee \to ee$, $ee \to \mu\mu$, $ee \to \tau\tau$, and $ee \to \nu_e \bar{\nu}_e Z$ (W boson fusion only, to avoid double-counting with $Z(\nu_e \bar{\nu}_e)Z$ events in the inclusive ZZ sample), while PYTHIA 8 was used for the production of other non-Higgs backgrounds (inclusive WW, ZZ, $Z/\gamma^*(q\bar{q})$ production). In the latter, PYTHIA 8 is responsible for both the matrix element calculation and the decays of unstable particles.

To be able to study separately the Higgs-strahlung and VBF processes in the $\nu\bar{\nu}jj$ final state, samples of ZH, $Z \to \nu_{\mu}\bar{\nu}_{\mu}$ were also produced. These samples, scaled by three times their nominal value of $\sigma \times \mathcal{B}$ to account for the number of neutrino flavours, were used to calculate the expected distributions of kinematic variables for the pure Higgs-strahlung component, while the component from VBF and interference between the two processes, was estimated as difference between the distribution from the $ee \to \nu_e \bar{\nu}_e H$ simulation and that of $ee \to ZH$, $Z \to \nu_{\mu}\bar{\nu}_{\mu}$.

4 Detector response and global event reconstruction

Generated events were passed through a parametric simulation of the detector response implemented in Delphes [31–33]. Tracks are assumed to be reconstructed with 100% efficiency for $p_T > 100 \,\mathrm{MeV}$ within an angular acceptance of 100 mrad in the IDEA tracking system. Track parameters are smeared according to the covariance matrix induced by the intrinsic detector resolution and by multiple scattering in the detector material [34]. Electromagnetic and hadronic energy deposits are smeared in the dual-readout calorimeters according to their nominal expected resolution.

A particle-flow (PF) algorithm uses the charged track candidates and the electromagnetic and hadronic energy deposits in the calorimeter to define three lists of reconstructed particle candidates: charged particles, photons and neutral hadrons. Electrons and muons with $E>2\,\mathrm{GeV}$ are assumed to be identified by dedicated algorithms with 99% efficiency, and a similar efficiency is assumed for photons. Particle misidentification is neglected. The missing momentum vector $\mathbf{p}^{\mathrm{miss}}$ is computed as the opposite of the vectorial sum of the momenta of all PF candidates.

The partons produced by the Higgs boson hadronic decays hadronise producing streams ("jets") of hadrons that interact with the detector. A jet clustering algorithm is used to combine the reconstructed particles into jet candidates. The jets' four-momenta are then calculated as the sum of the four-momenta of the jets' constituents. Jets are reconstructed with the exclusive "Durham" k_t algorithm [35], as implemented in FASTJET [36]. At each step, the two closest objects are merged until exactly N jets remain, with N=2 for $\ell\ell jj$ and $\nu\bar{\nu}jj$ events, and N=4 for jjjj events. The distance between two particles (or a particle and a jet) is defined as:

$$d_{ij} = 2\min(E_i^2, E_j^2)(1 - \cos\theta_{ij}). \tag{4.1}$$

The *E*-recombination scheme is adopted, and jets returned by the algorithm are sorted in decreasing order of their energies. The isolated leptons identified as the products of a $Z \to \ell\ell$ decay as described later are excluded from the inputs for the clustering.

To distinguish the flavour of the parton initiating a hadronic shower reconstructed as a jet, a tagging algorithm is used. This is based on a graph-neural-network algorithm exploiting various properties of the particle-flow inputs clustered into the jets. The main features of the algorithm are detailed in Ref. [34], though a more recent version [37] of its training is employed in this study. The network outputs seven scores, normalised to unity, corresponding to the probabilities that a jet originates from a b, c, s, u, or d quark, from a gluon, or from a hadronic decay of a τ lepton. The network was trained on independent simulated $Z(\nu\bar{\nu})H$ events, clustered into two jets with the same N=2 Durham algorithm as in the analysis. The true flavour label of each jet was derived from the generated Higgs decay.

5 The $\ell\ell jj$ final state

The analysis of the $\ell\ell jj$ ($\ell=e,\mu$) final state focuses on Higgs-strahlung events. While the analysis is optimised in ZH events, the contribution from Z-boson fusion is present, and represents <3% of the total number of expected Higgs events at $\sqrt{s}=240\,\mathrm{GeV}$ and $\sim27\%$ at $\sqrt{s}=365\,\mathrm{GeV}$ before the event selection. This channel has the best signal-to-background ratio among the three under study but the smallest expected yields, due to $\mathcal{B}(Z\to\ell\ell)=6.7\%$.

5.1 Event selection

Events are required to contain two leptons (electrons or muons)² of the same flavour and opposite-sign charges. The lepton momenta are required to be between the kinematic limits imposed by two-body kinematics and the Z boson boost in $e^+e^- \to ZH$ events: $25-80\,\text{GeV}$ (13 – 160 GeV) at $\sqrt{s}=240$ (365) GeV.

In case of multiple same-flavour, opposite-charge lepton pairs satisfying the previous requirements, the one with invariant mass closest to the nominal Z boson mass of 91.2 GeV is selected. The selected di-lepton pair is required to have invariant mass within a 20 GeV-wide range (81 - 101 GeV) around the nominal Z boson mass.

²charge conjugation is implicitly assumed

In ZH signal events, the Z boson is expected to recoil against a Higgs boson. By exploiting energy-momentum conservation and the knowledge of the initial 4-momentum of the collision, the recoil mass m_{recoil} can be calculated as:

$$m_{\text{recoil}}^2 = (\sqrt{s} - E_{l\bar{l}})^2 - p_{l\bar{l}}^2$$
 (5.1)

where $P_{\ell\ell} = (E_{\ell\ell}, \vec{p}_{\ell\ell})$ is the reconstructed four-momentum of the di-lepton pair. In ZH events, the recoil mass is expected to be peaked near the Higgs boson mass. Events are therefore required to pass the requirement $120 < m_{\text{recoil}} < 140 \text{ GeV}$.

After the lepton candidates from the $Z \to \ell\ell$ decays have been identified, jets are reconstructed by clustering all the p-flow candidates after excluding the two selected leptons.

A veto for events containing additional leptons with momenta above 25 GeV and a requirement that the variables $d_{2,3}$ and $d_{3,4}$ are greater than zero is applied to suppress background events from Higgs decays to non-hadronic final states, such as $H \to \tau\tau$ with one of the τ leptons decaying to leptons, from ZZ events and from inclusive $Z(\ell\ell)$ production.

The selection criteria, and the expected yields and efficiencies of each selection step for signal and background processes, are listed in Table 1 for $\sqrt{s} = 240 \,\text{GeV}$ (Table 6 shows the yields at $\sqrt{s} = 365 \,\text{GeV}$ in Appendix A).

The final selection efficiencies for $\ell\ell H$ events at $\sqrt{s}=240\,\mathrm{GeV}$ are 60%, 62%, 63%, 63% for Higgs bosons decaying to $b\bar{b}$, $c\bar{c}$, $g\bar{g}$, or $s\bar{s}$, respectively. The efficiency for other Higgs boson decays is 46% for WW, 54% for ZZ and 41% for $\tau\tau$; when only fully hadronic decays of the Higgs boson decay products are considered, the efficiency is 63% for WW, 59% for ZZ and 56% for $\tau\tau$.

Z-boson fusion events are estimated to contribute, after the selection, to only about 3% of the total signal.

At $\sqrt{s}=365\,\mathrm{GeV}$, the final efficiencies are around 50%, 54%, 54%, 54% for $\ell\ell H$ events with the Higgs boson decay respectively to $b\bar{b}$, $c\bar{c}$, $g\bar{g}$, or $s\bar{s}$, and 32%, 38%, 20% for the WW, ZZ and $\tau\tau$ decays. Considering only fully hadronic decays for these last three cases, the efficiencies are 55%, 51% and 47%, respectively.

The expected recoil mass distributions for signal and background processes superimposed after the selection are shown in Figure 1. At $\sqrt{s}=365\,\mathrm{GeV}$, the higher centre-of-mass energy, larger beam energy spread and larger lepton momenta lead to a wider signal distribution with a longer tail extending to higher values of the recoil mass. For a similar reason, the tail of the Z boson peak from $Z(\ell\ell)Z(q\bar{q})$ events extends to significantly higher values of m_{recoil} at $\sqrt{s}=365\,\mathrm{GeV}$, leading to a worse signal-to-background ratio S/B than at $\sqrt{s}=240\,\mathrm{GeV}$.

5.2 Event classification

After the selection described in the previous section, events at $\sqrt{s}=240~(365)\,\mathrm{GeV}$ are classified in ten (eleven) mutually orthogonal categories corresponding to the seven Higgs boson decays – to $b\bar{b}, c\bar{c}, s\bar{s}, gg, WW, ZZ$ and $\tau\tau$ – and the three (four) main background processes: $ZZ, WW, Z/\gamma^*(\ell\ell)$ (and $t\bar{t}$ at $\sqrt{s}=365~\mathrm{GeV}$). The classification is performed by a fully connected neural network (NN) with a number of input nodes equal to the number

Table 1: Selection criteria, expected yields and efficiency for signal and background processes for the $\ell\ell jj$ analysis, assuming an integrated luminosity $\mathcal{L}=10.8$ ab⁻¹ of e^+e^- collisions at $\sqrt{s}=240$ GeV. The equivalent yield at $\sqrt{s}=365$ GeV are shown in Appendix A, Table 6.

	$(qq)H\chi\chi$		$\ell\ell H(c\bar{c})$	(C)	$\ell\ell H(g)$	9)	$\ell\ell H(s\bar{s})$	(<u>s</u>	$\ell\ell H(WW)$	<u>~</u>	$\ell\ell H(ZZ)$	(·	$\ell\ell H(\tau\tau)$	Ē	ZZ		MM		$Z/\gamma^*(\ell$	()	$Z/\gamma^*(q)$	<u>(</u> 2
	Yield ε (%) Yield ε (%)	(%)	Yield ε	(%)	Yield ε	ε (%) 3	Yield ε (%)	(%)	Yield ε (%)		Yield ε (%)		Yield ε (%)	(%)	Yield ε	ε (%)	Yield	ε (%)	Yield ε	ε (%)	Yield ε	$\varepsilon~(\%)$
No cuts 87	87599		4348		12313		36	١.	32368		3971	'	9433	-	14677092		177535800		146804400	'	568662120	'
one $Z(\ell\ell)$ candidate 78	78728	06	3906	90	11058	06	32	06	29314	91	3594	91	8546	91	1223530	œ	1667859	П	28920864	20	304657	0
$m_{\ell\ell} \text{ in } 81101 \text{ GeV}$ 70	70832	06	3514	06	9948	06	29	06	26247	. 06	3244	90	7662	06	784799	64	410769	25	12264100	42	16264	5
$m_{\rm recoil} \text{ in } 120-140 \text{ GeV}$ 67	67630	95	3356	96	9502	96	28	96	24948	95	3059	94	7281	92	96931	12	179156	44	2014189	16	3161	19
no leptons with $p > 25 \text{ GeV}$ 64	64531	92	3325	66	9495	100	28	100	18326	73	2757	90	5398	74	87009	06	178913	100	2014187	100	2839	06
$d_{2,3} > 0, \ d_{3,4} > 0 \tag{64}$	64531	100	3325	100	9495	100	28	100	18136	66	2612	95	4781	88	69857	80	8072	23	71760	4	2839	100
$\ell = e \tag{31}$	31730		1633		4664	1	14		8904	ĺ	1284		2369		35366		5048	1	67285	'	1425	'
$\ell = \mu$ 32	32801	,	1692	,	4831	,	14	1	9232		1328	1	2412	,	34491	•	3024	1	4475	1	1414	1

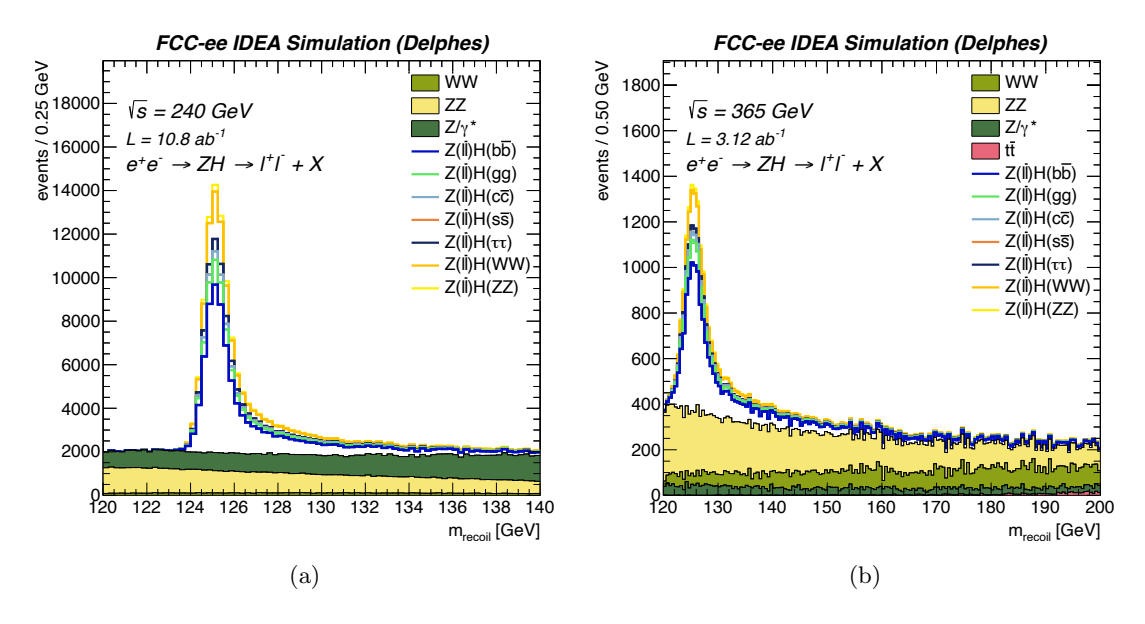


Figure 1: Recoil mass distribution of signal and background superimposed after the final selection for (a) $\sqrt{s} = 240 \,\text{GeV}$ and (b) $\sqrt{s} = 365 \,\text{GeV}$.

of input variables, four hidden layers (with respectively 128, 128, 128, and 64 nodes), and ten (eleven) output nodes corresponding to the target processes. The training of the neural network is performed with Keras [38] using the Tensorflow [39] backend. For the training, a subset of events is selected for each Higgs boson decay category from the signal samples, and for the background categories from the background samples. Two thirds of the events are used to train the network, and the other one third is used to validate it. Once trained, the network is evaluated on the full samples of Section 3.

The input variables used by the neural networks are the seven output scores $K_j = (b_j, c_j, s_j, g_j, \tau_j, u_j, d_j)$, j = 1, 2 of the flavour tagging algorithm [34, 37] for each of the two jets in the selected events (14 inputs), the di-jet invariant mass, the missing momentum, and the jet clustering distance variables $d_{2,3}$ and $d_{3,4}$.

In addition, the cosine of the polar angle $\theta_{\ell\ell}$ of the di-lepton pair is also included as an input of the neural network, to exploit the difference in angular distributions of the leptons from $Z \to \ell\ell$ decays in ZZ and ZH events due to the different spins of the Z (J=1) and Higgs (J=0) boson [40]. The training is performed over 50 epochs, after which the performance tends to saturate. The events are labelled as ZH(XX) $XX=b\bar{b},c\bar{c},s\bar{s},gg,WW,ZZ,\tau\tau$ or $ZZ,WW,Z/\gamma^*$ (and $t\bar{t}$ at $\sqrt{s}=365$ GeV) based on the output node of the NN with the largest score. The overall accuracy of the trained network is 80%, and no overtraining is observed. The migration matrices evaluated on the validation sample of the training are shown in Figure 2. The confusion among the target processes is slightly larger at $\sqrt{s}=365$ GeV due to the addition of one more target, the higher beam energy spread leading to worse signal/background separation.

To increase the final sensitivity of the analysis, the seven ZH(XX) categories are

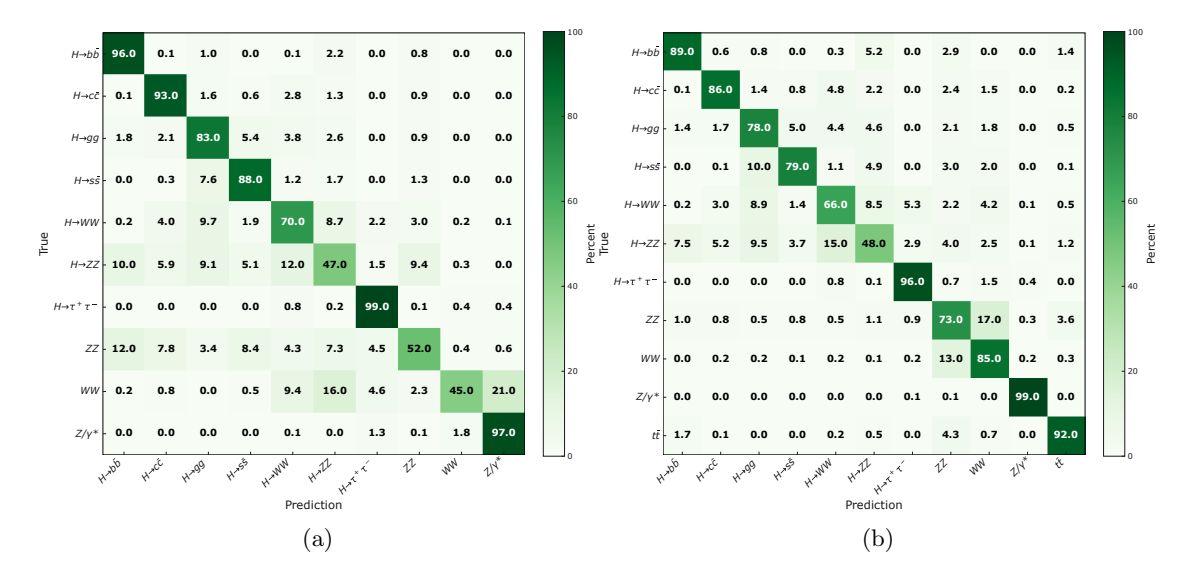


Figure 2: Confusion matrix of the NN after the final training, evaluated on the validation subsample, for (a) $\sqrt{s} = 240 \text{ GeV}$ and (b) $\sqrt{s} = 365 \text{ GeV}$.

further split into up to three subcategories based on the value of the NN output score of the events. The thresholds used to define the categories are chosen in order to maximise the expected combined significance summing in quadrature $S/\sqrt{S+B}$, where S and B are the signal and background yields in each category, leading to a total of up to 24 (25) categories at $\sqrt{s} = 240$ (365) GeV.

6 The $\nu \bar{\nu} j j$ final state

The analysis of the $\nu\bar{\nu}jj$ final state aims at extracting both ZH (with $Z \to \nu\bar{\nu}$) and VBF Higgs boson production events. This channel has the second best signal-to-background ratio among the three under study and an expected yield before selection that is about three times larger than the $\ell\ell jj$ final state, due to $\mathcal{B}(Z \to \nu\bar{\nu}) = 20\%$. The reconstructed final state contains two jets from the Higgs boson decays and large momentum imbalance due to the neutrinos from the Z boson decay. Hence, for signal events, the reconstructed di-jet invariant mass m_{jj} is expected to peak at the Higgs boson mass value, while the recoil mass of the di-jet system m_{recoil} is expected to peak at the Z boson mass value in Higgs-strahlung production and to accumulate at higher values in VBF events.

6.1 Event selection

Events containing at least one lepton with p > 20 GeV are vetoed. This requirement removes leptonic or semi-leptonic background events and ensures orthogonality with respect to the selection of the $\ell\ell jj$ analysis.

A loose preselection on the di-jet invariant mass $m_{jj} > 20 \,\text{GeV}$ is applied, in addition to a requirement on the recoil mass $m_{\text{recoil}} > 10 \,\text{GeV}$ that ensures orthogonality with the analysis of fully hadronic final states described in the next section. The cosine of

the angle between the visible momentum and the beam axis is required to satisfy the requirement $|\cos\theta_{jj}| < 0.85$ to suppress single and di-boson backgrounds. sFurthermore, requirements on $d_{1,2}$ and $d_{2,3}$ suppress events with a topology consistent with more than two well separated jets. The number of expected events after each step of the selection for signal and background processes is shown in Table 2.

Table 2: Yields after each step of the selection and final efficiency for each signal and background process for the $\nu\bar{\nu}jj$ analysis for VBF and ZH production modes, assuming an integrated luminosity $\mathcal{L} = 10.8 \text{ ab}^{-1}$ of e^+e^- collisions at $\sqrt{s} = 240 \text{ GeV}$. The equivalent yield table for $\sqrt{s} = 365 \text{ GeV}$ is shown in the Appendix A in Table 7.

	Yield	Yield	Yield after	Yield after	
Process	before	after	$ \cos\theta < 0.85$	kinematics & d_{ij}	Efficiency(%)
	selection	lepton veto	requirement	requirements	
$\nu_e \bar{\nu}_e H, H(b\bar{b})$	3.80×10^{4}	3.80×10^{4}	3.49×10^{4}	2.86×10^{4}	75.3
$\nu_e \bar{\nu}_e H, H(c\bar{c})$	1.90×10^{3}	1.90×10^{3}	1.86×10^{3}	1.53×10^{3}	80.5
$\nu_e \bar{\nu}_e H, H(gg)$	5.40×10^{3}	5.40×10^3	5.40×10^3	4.40×10^{3}	81.5
$\nu_e \bar{\nu}_e H, H(s\bar{s})$	1.57×10^{1}	1.57×10^{1}	1.58×10^{1}	1.28×10^{1}	81.5
$\nu_e \bar{\nu}_e H, H(\tau \tau)$	3.60×10^{3}	3.60×10^{3}	2.59×10^{3}	2.00×10^{3}	55.6
$\nu_e \bar{\nu}_e H, H(WW)$	1.37×10^{4}	1.37×10^4	9.70×10^{3}	7.80×10^{3}	56.9
$\nu_e \bar{\nu}_e H, H(ZZ)$	1.64×10^{3}	1.64×10^{3}	1.44×10^{3}	1.14×10^{3}	69.5
$ZH, H(bar{b})$	2.52×10^{5}	2.52×10^5	2.31×10^5	5.40×10^{4}	79.2
$ZH, H(c\bar{c})$	1.25×10^{4}	1.25×10^{4}	1.22×10^{4}	1.05×10^{4}	84.3
ZH, H(gg)	3.54×10^4	3.54×10^{4}	3.54×10^{4}	3.06×10^{4}	86.4
$ZH, H(sar{s})$	1.04×10^{2}	1.04×10^{2}	1.04×10^{2}	8.97×10^{1}	86.2
ZH, H(au au)	2.37×10^4	2.37×10^{4}	1.71×10^{4}	1.37×10^{4}	57.7
ZH, H(WW)	9.00×10^4	9.00×10^{4}	6.36×10^{4}	5.40×10^{4}	60.0
ZH, H(ZZ)	1.08×10^{4}	1.08×10^{4}	9.54×10^{3}	7.80×10^{3}	72.2
qqH	5.76×10^{5}	5.76×10^5	4.92×10^5	2.60×10^{4}	3.84
WW	1.73×10^{8}	1.73×10^8	1.06×10^{8}	1.37×10^7	7.51
ZZ	1.40×10^{7}	1.40×10^7	1.10×10^7	2.67×10^{6}	18.8
$Z/\gamma^* o q\bar{q}$	5.66×10^{8}	5.66×10^8	5.47×10^8	5.85×10^{6}	1.01

Figure 3 (4) shows the recoil mass and the di-jet invariant mass distributions of signal and background events passing the pre-selection at $\sqrt{s} = 240 \,\text{GeV}$ ($\sqrt{s} = 365 \,\text{GeV}$).

6.2 Event classification

Seven event-wise flavour-tagging observables $K = K_1 + K_2$, K = (B, C, S, G, T, U, D), are calculated from the sum of the flavour probabilities K_j (j = 1, 2) of the two reconstructed jets as determined by the jet flavour tagging algorithm. The K-scores are then used to classify the events into seven orthogonal "K-like" categories according to the score with the largest value. The corresponding migration matrix for the signal-like (K = B, C, S, G) categories is shown in Figure 5, exhibiting small confusion across different signals. Categories containing jet pairs tagged as K = T, U, D are discarded.

Events in each of the four K-like categories (K = B, C, S, G) are further classified, based on the value of the K-score, in three orthogonal categories with varying signal purity: low (LP), medium (MP) and high (HP) purity, thus leading to a total of 12 categories. The

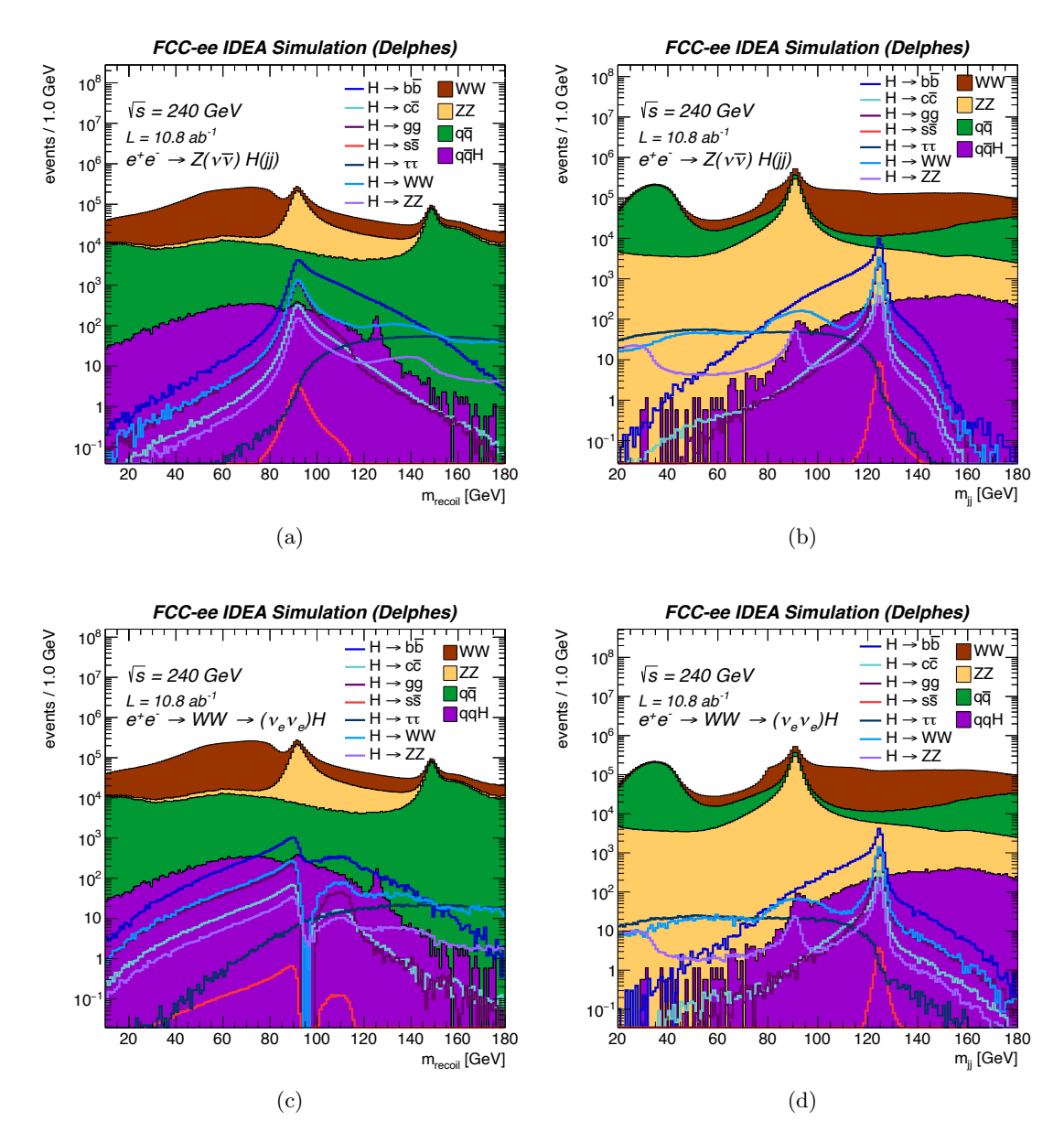


Figure 3: The m_{recoil} and the di-jet invariant mass m_{jj} distributions after pre-selection for the ZH production mode (a,b) and for the VBF production mode (c,d) at $\sqrt{s} = 240 \,\text{GeV}$.

criteria to choose the thresholds on the K-scores that define LP, MP and HP categories were optimised by maximising the individual significance for each signal in their respective enriched category.

7 The jjjj final state

The analysis of the jjjj final state targets the ZH production mode with both Z and Higgs bosons decaying to pairs of partons. Among the three channels under study, despite

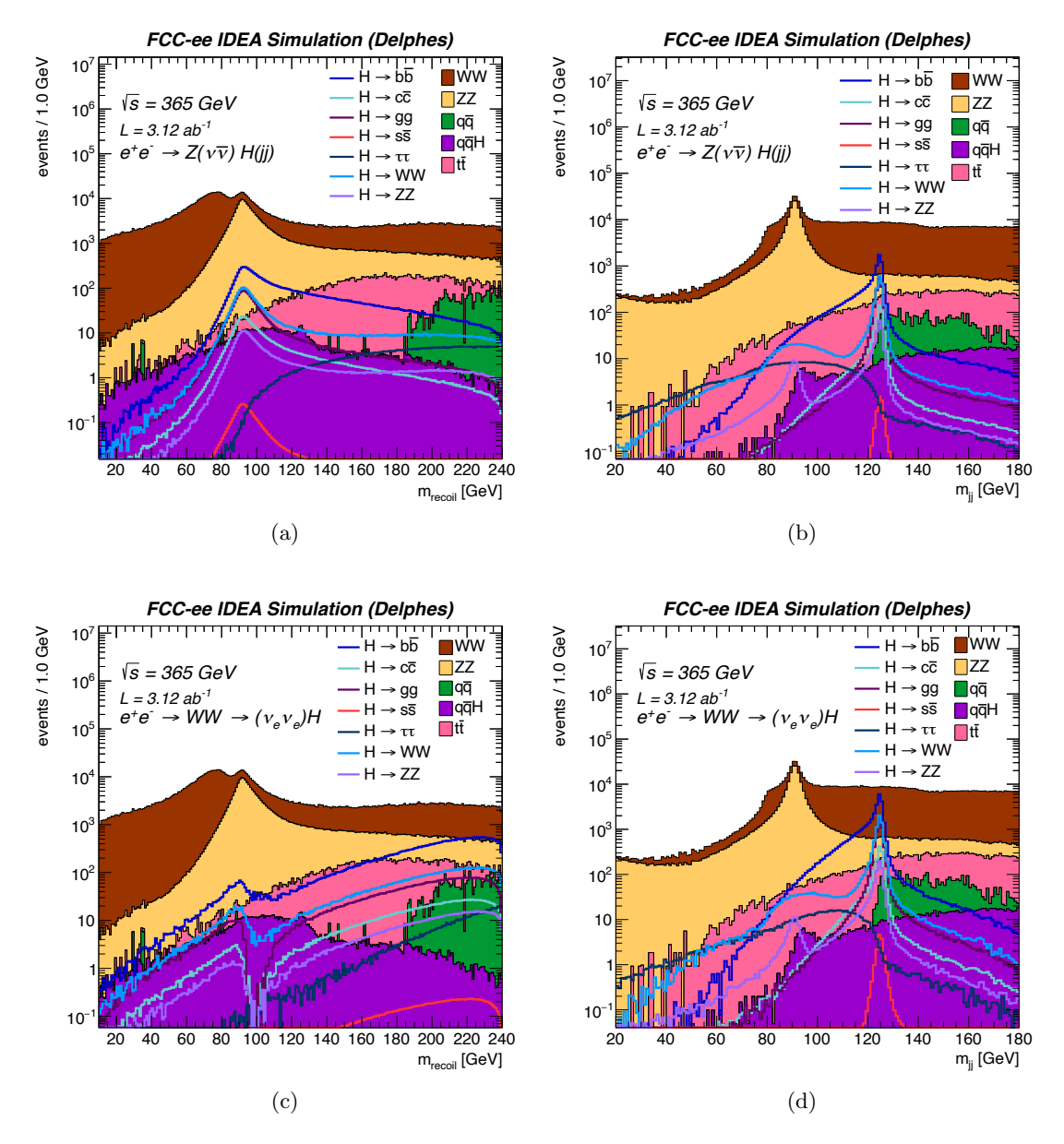


Figure 4: The m_{recoil} and the di-jet invariant mass m_{jj} distributions after pre-selection for the ZH production mode (a,b) and for the VBF production mode (c,d) at $\sqrt{s} = 365 \,\text{GeV}$.

the larger expected event yield, the jjjj one features the worst signal-to-background ratio and presents challenges in jet clustering and resolving the ambiguity on the jet origin.

7.1 Event selection

Events containing at least one lepton $(e \text{ or } \mu)$ with p > 20 GeV are vetoed, for orthogonality with respect to the $\ell\ell jj$ analysis. To reject $\nu\bar{\nu} jj$ events, a selection requirement on the visible mass, $m_{\text{vis}} > 150 \text{ GeV}$ is applied. All the visible particles are clustered in four exclusive jets with the Durham algorithm. The cosine of the angle between the visible

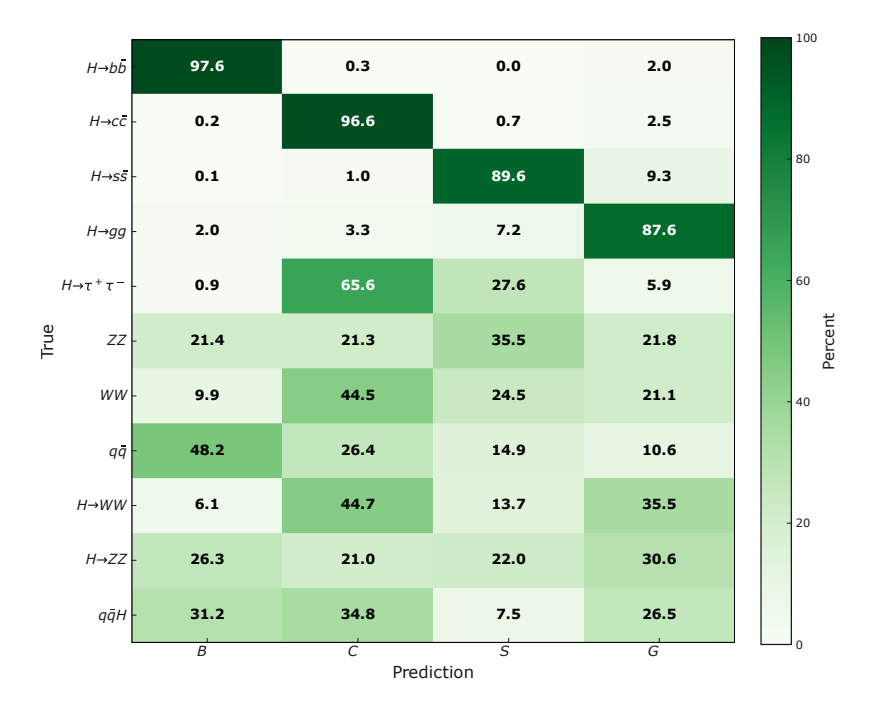


Figure 5: Migration matrix in the four categories of interest, for the $\nu\bar{\nu}jj$ analysis at $\sqrt{s} = 240$ GeV. The numbers correspond to the fraction of events (in percent) of a given process (vertical axis) after the preselection, that are classified in one of the four K-like categories (horizontal axis).

momentum and the beam axis is required to be $|\cos \theta_{\text{vis}}| < 0.85$ to reject single and diboson backgrounds. Additional requirements on the $d_{1,2}$, $d_{2,3}$ and $d_{3,4}$ merge distance variables are applied such that a four jet topology is selected.

The measurement of the reconstructed jet energies $(E_i, i = 1..4)$ is improved by exploiting four-momentum conservation, the known initial-state four-momentum $(\sqrt{s}, \vec{0})$, and the jet directions $\vec{\beta}_i = \vec{p}_i/E_i$, solving the following system of four equations:

$$\begin{bmatrix} 1 & 1 & 1 & 1 \\ \beta_1^x & \beta_2^x & \beta_3^x & \beta_4^x \\ \beta_1^y & \beta_2^y & \beta_3^y & \beta_4^y \\ \beta_1^z & \beta_2^z & \beta_3^z & \beta_4^z \end{bmatrix} \begin{bmatrix} E_1 \\ E_2 \\ E_3 \\ E_4 \end{bmatrix} = \begin{bmatrix} \sqrt{s} \\ 0 \\ 0 \\ 0 \end{bmatrix}$$

The solution of the system is performed via a numerical inversion of the matrix. A χ^2 is computed from the values of the jet energies before and after the matrix inversion, assuming a jet energy resolution of $50\%/\sqrt{E}$. Events with values of χ^2 above a certain threshold are vetoed suppressing events with poor jet energy reconstruction.

The yields and efficiency of the selection after each step, for signal and background processes, are shown in Table 3.

Table 3: Expected event yields and efficiencies (in %) for signal and background processes, after each step of the jjjj event selection, assuming an integrated luminosity $\mathcal{L}=10.8~\mathrm{ab}^{-1}$ of e^+e^- collisions at $\sqrt{s}=240~\mathrm{GeV}$. Yields at $\sqrt{s}=365~\mathrm{GeV}$ are shown in Table 8 in Appendix A. Here, $Z(q\bar{q})$ in ZH processes denotes Z boson decays to $u\bar{u}$ and $d\bar{d}$. Inclusive samples for $\nu\bar{\nu}H$, e^+e^-H and $\mu^+\mu^-H$ are included showing the orthogonality between the analyses.

	Yield	Yield	Yield after	Yield after	Yield after	
Process	before	after	$m_{\rm vis}, \theta_{\rm vis}$	$d_{ m ij}$	χ^2	Efficiency (%
	selection	lepton veto	requirement	requirement	requirement	
$Z(c\bar{c})H(gg)$	2.06×10^{4}	2.06×10^{4}	2.04×10^{4}	1.81×10^{4}	1.72×10^{4}	83.5
$Z(c\bar{c})H(s\bar{s})$	6.06×10^{1}	6.06×10^{1}	5.99×10^{1}	5.32×10^{1}	5.01×10^{1}	82.7
$Z(c\bar{c})H(c\bar{c})$	7.29×10^{3}	7.29×10^3	7.04×10^{3}	6.38×10^{3}	5.89×10^3	80.8
$Z(car{c})H(bar{b})$	1.47×10^{5}	1.47×10^{5}	1.32×10^{5}	1.21×10^{5}	1.06×10^{5}	72.1
$Z(q\bar{q})H(gg)$	4.72×10^{4}	4.72×10^{4}	4.71×10^{4}	4.05×10^{4}	3.92×10^4	83.1
$Z(q\bar{q})H(s\bar{s})$	1.38×10^{2}	1.38×10^{2}	1.38×10^{2}	1.19×10^{2}	1.14×10^{2}	82.6
$Z(q\bar{q})H(c\bar{c})$	1.67×10^{4}	1.67×10^4	1.63×10^{4}	1.44×10^{4}	1.36×10^{4}	81.4
Z(qar q)H(bar b)	3.36×10^{5}	3.36×10^5	3.07×10^5	2.79×10^{5}	2.48×10^5	73.8
$Z(bar{b})H(gg)$	2.65×10^{4}	2.65×10^4	2.51×10^4	2.29×10^4	2.08×10^{4}	78.5
$Z(bar{b})H(sar{s})$	7.77×10^{1}	7.77×10^1	7.38×10^{1}	6.74×10^{1}	6.02×10^{1}	77.5
$Z(bar{b})H(car{c})$	9.36×10^{3}	9.36×10^3	8.61×10^3	7.96×10^{3}	6.98×10^{3}	74.6
$Z(bar{b})H(bar{b})$	1.88×10^{5}	1.88×10^5	1.59×10^5	1.49×10^{5}	1.23×10^{5}	65.4
$Z(s\bar{s})H(gg)$	2.65×10^{4}	2.65×10^4	2.64×10^4	2.29×10^4	2.22×10^4	83.8
$Z(s\bar{s})H(s\bar{s})$	7.77×10^{1}	7.77×10^{1}	7.76×10^1	6.72×10^{1}	6.46×10^{1}	83.1
$Z(s\bar{s})H(c\bar{c})$	9.35×10^{3}	9.35×10^3	9.15×10^3	8.14×10^3	7.67×10^3	82.0
$Z(s\bar{s})H(b\bar{b})$	1.88×10^{5}	1.88×10^5	1.72×10^5	1.57×10^5	1.40×10^5	74.5
$Z(b\bar{b})H(au au)$	2.03×10^{4}	2.03×10^4	1.29×10^4	7.34×10^3	2.38×10^3	11.7
$Z(c\bar{c})H(au au)$	1.58×10^{4}	1.58×10^4	1.06×10^4	6.35×10^3	2.14×10^3	13.5
$Z(s\bar{s})H(au au)$	2.03×10^{4}	2.03×10^4	1.38×10^{4}	8.55×10^3	2.88×10^3	14.2
$Z(q\bar{q})H(au au)$	3.61×10^{4}	3.61×10^4	2.45×10^4	1.52×10^4	5.12×10^3	14.2
$Z(b\bar{b})H(Z\gamma)$	4.96×10^{2}	4.96×10^2	4.29×10^2	3.06×10^2	2.72×10^2	54.8
$Z(c\bar{c})H(Z\gamma)$	3.86×10^{2}	3.86×10^2	3.50×10^2	2.45×10^2	2.27×10^2	58.8
$Z(s\bar{s})H(Z\gamma)$	4.96×10^{2}	4.96×10^2	4.55×10^2	3.12×10^2	2.93×10^{2}	59.1
$Z(q\bar{q})H(Z\gamma)$	8.68×10^{2}	8.68×10^2	7.95×10^2	5.42×10^2	5.09×10^2	58.6
$Z(b\bar{b})H(WW)$	6.97×10^{4}	6.97×10^4	4.51×10^{4}	3.83×10^{4}	2.73×10^{4}	39.2
$Z(c\bar{c})H(WW)$	5.42×10^{4}	5.42×10^4	3.69×10^{4}	3.11×10^4	2.28×10^{4}	42.1
$Z(s\bar{s})H(WW)$	6.96×10^{4}	6.96×10^4	4.79×10^{4}	4.00×10^{4}	2.95×10^{4}	42.4
$Z(q\bar{q})H(WW)$	1.24×10^{5}	1.24×10^5	8.51×10^{4}	7.07×10^{4}	5.21×10^{4}	42.0
$Z(b\bar{b})H(ZZ)$	8.55×10^{3}	8.55×10^3	6.99×10^{3}	4.99×10^{3}	3.60×10^3	42.1
$Z(c\bar{c})H(ZZ)$	6.66×10^{3}	6.66×10^3	5.73×10^3	4.07×10^3	3.04×10^3	45.6
$Z(s\bar{s})H(ZZ)$	8.54×10^{3}	8.54×10^3	7.48×10^{3}	5.29×10^{3}	3.99×10^{3}	46.7
$Z(q\bar{q})H(ZZ)$	1.52×10^{4}	1.52×10^4	1.33×10^4	9.36×10^3	7.06×10^3	46.4
W^+W^-	1.64×10^{8}	1.64×10^{8}	1.05×10^{8}	6.92×10^{7}	5.85×10^{7}	35.7
ZZ	1.36×10^{7}	1.36×10^{7}	1.09×10^{7}	5.69×10^{6}	4.69×10^{6}	34.5
$qar{q}$	5.65×10^{8}	5.65×10^{8}	5.45×10^{8}	1.04×10^{8}	4.02×10^{7}	7.1
$e^{+}e^{-}H$	7.66×10^4	7.66×10^{4}	1.81×10^{2}	1.13×10^{2}	0.0	0.0
$\mu^+\mu^-H$	7.21×10^4	7.21×10^4	9.42×10^{1}	3.68×10^{1}	0.0	0.0
$ u\bar{\nu}H$	4.71×10^{5}	4.71×10^{5}	4.12×10^{5}	2.29×10^{2}	0.0	0.0

7.2 Event classification

After the previous preselection, the four jets are combined pair-wise to form the Higgs and Z boson candidates. The procedure, illustrated in Figure 6, proceeds as follows:

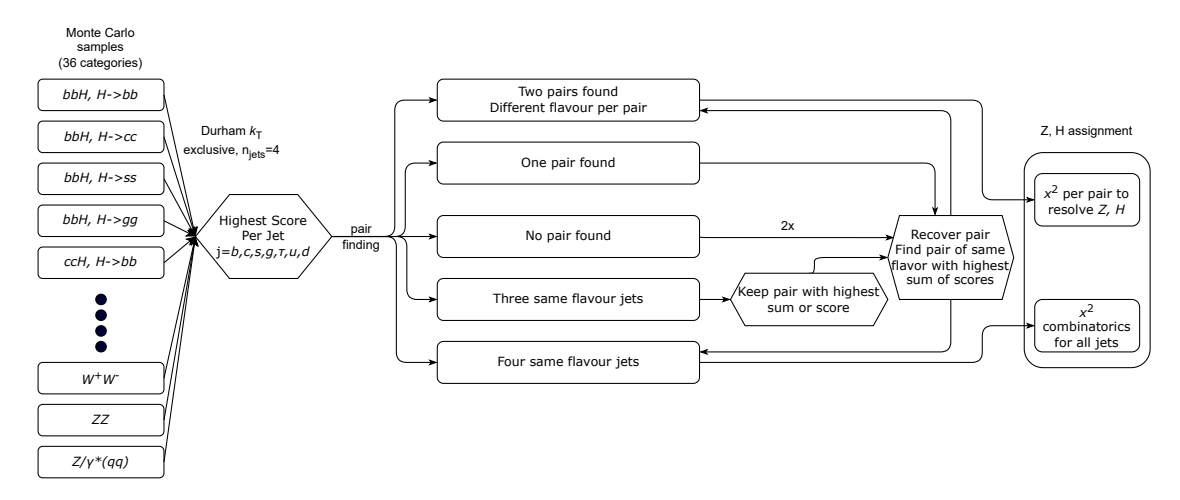


Figure 6: Illustration of the jet pairing procedure in the fully-hadronic analysis.

- First, the flavour of the four jets is determined. Each reconstructed jet i is initially assigned a flavour corresponding to the highest K_i -score from the flavour tagging algorithm ($K = b, c, s, g, \tau, u, d$). If the event does not contain two pairs of jets with the same predicted flavour, a recovery procedure is performed:
 - (a) If there is one pair of jets with the same flavour, while the remaining two have different flavours (e.g. b, b, g, c), the sum of the K-scores of the two different flavour jets is computed for each hypothesis $K = u, d, s, c, b, g, \tau$. The two jets are then assigned the flavour hypothesis that maximises this sum.
 - (b) If no pair of jets shares the same flavour (e.g. b, g, c, s), the procedure above is applied twice: first to identify the jet pair and flavour hypothesis that yield the highest total K-score among all possible pairings, and then again to the remaining pair of jets.
 - (c) If three jets share the same flavour (e.g. b, b, b, c), the pair among the three identical-flavour jets with the highest combined K-score for that flavour hypothesis is retained. The remaining pair of jets is then assigned the flavour hypothesis that maximises the sum of their K-scores.
- After the previous steps, the events contain two pairs of same-flavoured jet. The assignment of each jet either a parent Z or Higgs boson depends on whether the pairs are of same or different flavour:
 - (a) if the pairs have different flavour, then one pair is considered to originate from the Z boson and the other one from the Higgs boson, choosing the configuration

that minimises $\chi^2 = (m_{j_1j_2} - m_Z)^2 + (m_{j_3j_4} - m_H)^2$, where $m_{j_1j_2}$, $m_{j_3j_4}$, are the di-jet invariant masses and m_Z, m_H are the Z and Higgs boson masses $(m_Z = 91.2 \,\text{GeV})$ and $m_H = 125 \,\text{GeV})$.

(b) if all four jets are of the same flavour, then all possible pairs of jets are considered, and the configuration that minimises $\chi^2 = (m_{j_1j_2} - m_Z)^2 + (m_{j_3j_4} - m_H)^2$ is chosen.

At the end of the procedure, the four jets are thus grouped into two pairs of jets of same flavour, considered to be candidates $Z(Z_{jj})$ or Higgs (H_{jj}) boson decays. To further suppress WW and ZZ background events, the following requirements are applied:

$$\sqrt{(m_{Z_{jj}} - m_W)^2 + (m_{H_{jj}} - m_W)^2} > 10 \text{ GeV}, \tag{7.1}$$

$$\sqrt{(m_{Z_{jj}} - m_Z)^2 + (m_{H_{jj}} - m_Z)^2} > 10 \text{ GeV}, \tag{7.2}$$

where $m_W = 80.377 \,\text{GeV}$ is the W boson mass. Finally, $m_{Z_{jj}}$ and $m_{H_{jj}}$ are required to be in the following ranges: 50 $\,\text{GeV} < m_{Z_{jj}} < 125 \,\,\text{GeV}$, and 91 $\,\text{GeV} < m_{H_{jj}} < 180 \,\,\text{GeV}$. The $m_{Z_{jj}}$ and $m_{H_{jj}}$ distributions of signal and background events passing the selection are shown in Figure 7.

Events passing the previous requirements are classified in 16 orthogonal regions (BB, BC, ...) based on the flavours assigned to the two jet pairs. Events in which the Higgs boson decay products are tagged as τ leptons are rejected, suppressing more than 95% of $H \to \tau \tau$ events. The corresponding migration matrix is shown in Figure 8.

The events in each of the 16 regions are further classified into three orthogonal categories of low (LP), medium (MP) and high (HP) signal purity based on selections on the sum of the K-scores for the two jet pairs, leading to a total of 48 categories. The boundaries that define LP, MP and HP categories were chosen by maximising the individual significance for each signal in their respective enriched category.

8 Signal strength measurement

One- or two-dimensional distributions of discriminant variables in pseudo-data samples at $\sqrt{s} = 240$ or 365 GeV in the categories of the three different channels are interpreted simultaneously in terms of signal strengths of the Higgs boson production and decay processes under study through a binned maximum likelihood fit.

Pseudo-data samples are obtained by summing together the histograms of the discriminant variables for each signal and background process, scaled to the assumed value of the integrated luminosity given the SM cross-sections and branching ratios of each process.

In each category, the likelihood function is constructed as the product of Poisson probabilities over all bins of the histogram of the corresponding discriminant variable(s), where the observed count in the pseudo-data sample is compared to the expected yield from the sum of signal and background. The likelihood function at each centre-of-mass energy is calculated as the product of the likelihood functions for the categories of the three final states under study.

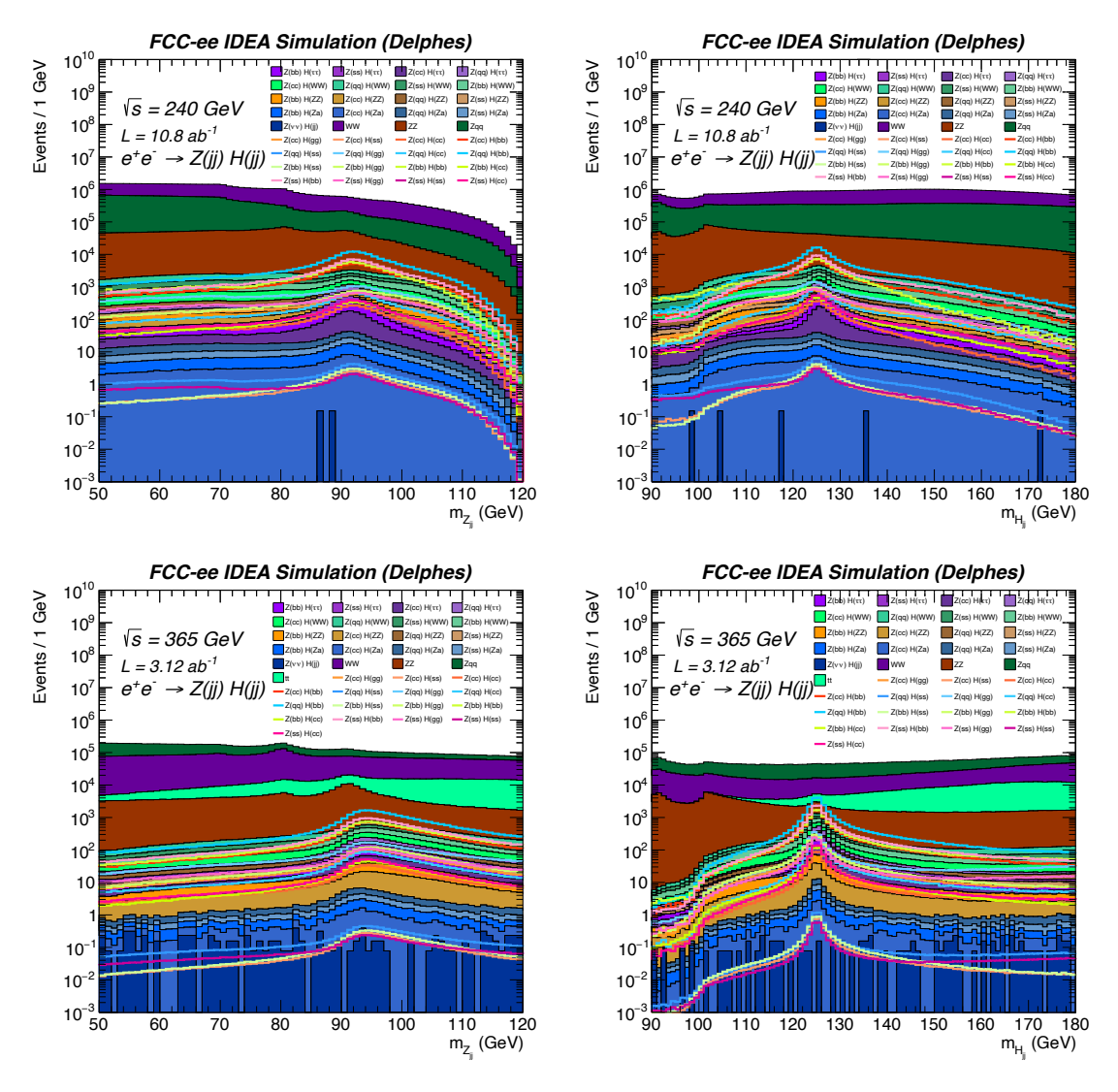


Figure 7: Distribution of di-jet invariant mass m_{jj} of the jets associated to the Z (left) and to the H (right) bosons for $\sqrt{s} = 240 \,\text{GeV}$ (top) and $\sqrt{s} = 365 \,\text{GeV}$ (bottom).

The yields for each Higgs boson decay mode in each bin are calculated as the product of the expected yield times a signal strength μ_{XX} . Separate signal strengths are assigned to each Higgs boson decay mode XX under study: $b\bar{b}$, $c\bar{c}$, $s\bar{s}$, gg. The large control regions (categories targeting background processes or Higgs boson decays other than those under study) and the sidebands of the discriminant variable distributions in the categories targeting the signal processes allow fitting also the normalisations of other Higgs boson decays ($\tau\tau$, WW and ZZ) and of the main background processes. Tests showed that, allowing them to float freely or constraining them with a prior at the few-percent level, yields consistent results and hence are left floating.

The discriminant variables used in the fit in each channel are the following:

• $\ell\ell jj$ final state: one-dimensional distributions of the recoil mass $(m_{\rm recoil})$ in the in-



Figure 8: Migration matrix of the full hadronic final state. Each row corresponds to a different process. The 16 columns show the fractions of events in these jet combinations entering the fit. For example SB would include events tagged as $Z \to s\bar{s}$, $H \to b\bar{b}$. Events where Higgs boson decays are tagged as $\tau\tau$ are removed.

terval 120-140 GeV, with a bin width of 0.25 GeV, are used.

- $\nu\bar{\nu}jj$ final state: two-dimensional distributions of the recoil mass $(m_{\rm recoil})$ versus the di-jet invariant mass $(m_{\rm jj})$ are used. The ranges for $m_{\rm jj}$ and $m_{\rm rec}$ are $50-180\,{\rm GeV}$ (50 180) and $20-200\,{\rm GeV}$ (20 280) for $\sqrt{s}=240$ (365) GeV, with bin widths of 1 GeV and 5 GeV respectively.
- jjjj final state: two-dimensional distributions of the di-jet invariant masses $m_{H_{jj}}$ and $m_{Z_{jj}}$ are used, in the ranges of $90-180\,\text{GeV}$ and $50-120\,\text{GeV}$, with bin widths of $1\,\text{GeV}$ and $5\,\text{GeV}$ respectively.

In the $\nu \bar{\nu} j j$ final state, separate distributions of m_{jj} vs m_{recoil} and signal strengths are included in the fit for the ZH and VBF production modes, exploiting the expected differences in these distributions for the two production modes to distinguish among them.

Uncertainties from the finite size of simulated samples are incorporated in the fit using the Beeston–Barlow method [41]. Shape systematic uncertainties from background modelling, as well as experimental uncertainties related to event selection and flavour tagging, are not included. Large control samples at FCC-ee and improvements in theoretical calculations in the next two decades will allow the shapes and normalisations of these processes to be constrained with an accuracy at the permille level.

The uncertainties in the signal strengths for the Higgs boson decay modes under study and the other Higgs boson decays expected from each individual channel, when inputs from the other channels are not included in the fit, are summarised in Table 4. The uncertainties expected when the three channels are combined together are shown in Table 5.

Signal strengths for the Higgs boson decay modes that are backgrounds to those under study are constrained to precisions that are at best 1.1% ($H \to WW$), 2.5% ($\tau\tau$) and 6.9% (ZZ) for ZH production at $\sqrt{s}=240$ GeV. Dedicated measurements targeting these processes as signals will achieve significantly better precision.

Table 4: Relative uncertainty (%) for $\sigma_{ZH} \times \mathcal{B}(H \to XX)$ and $\sigma_{\nu_e \bar{\nu}_e} \times \mathcal{B}(H \to XX)$ at 68 % CL for the individual $\ell\ell jj$, $\nu\nu jj$, and jjjj final states, assuming integrated luminosities of $\mathcal{L}=10.8~\mathrm{ab^{-1}}$ at $\sqrt{s}=240~\mathrm{GeV}$ and $\mathcal{L}=3.12~\mathrm{ab^{-1}}$ at $\sqrt{s}=365~\mathrm{GeV}$.

Final State	1	jj		ν̄ν	jj		jj	jj
$\sqrt{s} \; (\mathrm{GeV})$	240	365	2	40	30	65	240	365
Channel	Z	Н	ZH	$\nu_e \bar{\nu}_e H$	ZH	$\nu_e \bar{\nu}_e H$	Z	H
$H o b ar{b}$	±0.60	± 1.30	± 0.38	± 1.99	± 0.70	± 0.65	± 0.32	± 0.54
$H \to c\bar{c}$	± 3.47	± 9.3	± 2.66	± 21	± 4.72	± 3.42	± 3.52	± 4.59
$H\to s\bar s$	± 220	± 880	±159	± 1000	±460	± 283	±480	± 690
$H \to gg$	± 1.93	± 4.43	± 1.06	± 5.7	± 2.89	± 2.58	± 3.07	± 4.28

Table 5: Relative uncertainty (%) for $\sigma_{ZH} \times \mathcal{B}(H \to XX)$ and $\sigma_{\nu_e \bar{\nu}_e} \times \mathcal{B}(H \to XX)$ at 68% CL combining the $\ell\ell jj$, $\nu\nu jj$, and jjjj final states.

\sqrt{s}	240	${ m GeV}$	365	${ m GeV}$
$\mathcal L$	10.8	${\rm ab^{-1}}$	3.12	ab^{-1}
Channel	ZH	$\nu_e \bar{\nu}_e H$	ZH	$\nu_e \bar{\nu}_e H$
$H o b ar{b}$	±0.21	± 1.89	±0.39	± 0.64
$H \to c\bar{c}$	± 1.75	± 20	± 3.01	± 3.36
$H\to s\bar s$	±110	± 990	±340	± 280
$H \to gg$	± 0.85	± 5.5	± 2.13	± 2.56

9 Conclusion

A study of the sensitivity to the measurement of the signal strengths for Higgs boson decays to $b\bar{b}$, $c\bar{c}$, gg and $s\bar{s}$ in ZH and VBF events using $\ell\ell jj$ ($\ell=e,\mu$), $\nu\bar{\nu}jj$ and jjjj final states af FCC-ee has been presented. The results assume an integrated luminosity of $10.8\,\mathrm{ab}^{-1}$ at $\sqrt{s}=240\,\mathrm{GeV}$ and $3.12\,\mathrm{ab}^{-1}$ at $\sqrt{s}=365\,\mathrm{GeV}$ of e^+e^- collisions, reconstructed by assuming four detectors with performance identical to that of the IDEA detector concept.

The combination of the three final states leads to expected uncertainties in the ZH production signal strength of 0.21%, 1.75%, 0.85%, 110% for $H \to b\bar{b}$, $H \to c\bar{c}$, $H \to gg$ and $H \to s\bar{s}$ decays at $\sqrt{s} = 240\,\mathrm{GeV}$, while the uncertainties are 2–3 times worse at 365 GeV due to the lower integrated luminosity and signal cross-section. Significant contribution to the $\nu\bar{\nu}H$ final state, especially at $\sqrt{s} = 365\,\mathrm{GeV}$, is expected from W-boson fusion events where the colliding beam particles emit a neutrino-antineutrino pair and two W bosons that fuse into a Higgs boson. A dedicated analysis that measures separately the $Z(\nu\bar{\nu})H$ and $\nu_e\bar{\nu}_eH$ contributions for the first time, yields an expected precision on the $\nu_e\bar{\nu}_eH$ signal strength below one % for $H \to b\bar{b}$ and few-% level for $H \to c\bar{c}$ and $H \to gg$ at $\sqrt{s} = 365\,\mathrm{GeV}$.

This work constitutes the first sensitivity study of the measurements of all major hadronic Higgs decay modes in a combined fit at the FCC-ee, simultaneously accounting for both ZH and VBF production processes, and including a full treatment of interference effects in the $\nu\bar{\nu}jj$ final state. The combination of results at $\sqrt{s}=240$ and 365 GeV with full covariance across all production and decay modes provides the expected FCC-ee sensitivity to hadronic Higgs decays, delivering percent to per-mille level precision for the dominant channels. For the first time, the sensitivity to the rare decay $H \to s\bar{s}$ is investigated in a global fit together with the other hadronic modes, demonstrating that FCC-ee could potentially provide evidence of the strange quark Yukawa coupling. Together with the precise determination of the total Higgs production cross-section from the recoil mass method [24], these results provide an essential input to model-independent Higgs coupling fits and to the extraction of the total Higgs width at the FCC-ee [21].

A Appendix

The distributions of selected NN input variables for the $\ell\ell jj$ analysis are shown in Figures 9–10.

The correlation matrices between the fitted signal strengths for the two Higgs boson production and four decay modes under study are shown in Figure 11 for both $\sqrt{s} = 240$ and 365 GeV.

The yields for the $\ell\ell jj$, $\nu\bar{\nu}jj$ and jjjj analysis at $\sqrt{s}=365\,\mathrm{GeV}$ are shown in Tables 6, 7 and 8 respectively.

Acknowledgments

This work was funded in part by the U.S. Department of Energy, Office of Science, Office of High Energy Physics under Contract No. DE-SC0012704. We would like to thank our

Table 6: Selection criteria, expected yields and efficiency for signal and background processes for the $\ell\ell jj$ analysis, assuming an integrated luminosity $\mathcal{L}=3.12~\mathrm{ab^{-1}}$ of e^+e^- collisions at $\sqrt{s}=365~\mathrm{GeV}.$

Selection	$\theta H(t)$	q	$\ell\ell H(b\bar{b})$ $\ell\ell H(c\bar{c})$	$c\bar{c}$	$\ell\ell H($	H(gg)	$\ell\ell H(s\bar{s})$	<u>is</u>	$\ell\ell H(WW)$	(A)	$\ell\ell H(ZZ)$	(Z.	$\ell\ell H(\tau \tau)$	÷	ZZ		WW	7	$t\bar{t}$		$Z/\gamma^*(\ell$	()	$Z/\gamma^*(q\bar{q})$	(F)
	Yield	(%) 3	Yield ε (%) Yield ε (%) Yield	ε (%)		ε (%)	Yield ε (%)	(%)	Yield ε	ε (%) Y	Yield ε (%)		Yield ε (%)	(%)	Yield ε (%)	٤ (%)	Yield	ε (%)	Yield	ε (%)	Yield ε (%)	ε (%)		
No cuts	21032		1044		2956	,	× ×		7771		957		2271	- 2	2005536		33435480		2496000		11909040		51224441	
> 0 iso-leptons with $p > 40$ GeV	7 20710	86	1028	86	2911	86	œ	86	7672	66	940	66	2237	66	371476	19	12313369	37	634365	25	9890946	85	56782	_
one $Z(\ell\ell)$ candidate	19255	93	953	93	2692	93	œ	93	7155	93	876	93	2103	93	271476	73	763372	9	94082	15	6235314	64	41193	1
$m_{\ell\ell}$ in 81–101 GeV	12780	99	629	99	1775	99	20	99	4757	99	595	89	1391	29	167446	62	66290	6	12271	13	2941287	47	26	
$m_{ m recoil}$ 120–200 GeV	11468	06	569	06	1609	91	20	91	4239	68	518	87	1241	88	37196	22	24020	36	541	4	286317	10	0	
$E(j_2) > 15 \text{ GeV}$	11435	100	568	100	1608	100	ro	100	4028	92	472	91	941	92	34910	94	22461	94	537	66	203444	71	0	
≤ 2 iso. leptons	10522	92	561	66	1597	66	ಸಂ	100	2536	63	383	81	482	51	30989	88	22324	66	495	92	203444	100	0	
$d_{23} > 0, d_{34} > 0$	10522	100	561	100	1597	100	20	100	2532	100	364	92	466	96	25410	85	11856	53	495	100	4980	2	0	
$\ell = e$	5223	١.	278		789		2	١.	1254		180		232		13179	١.	6269	'	253		3780		0	
$\ell=\mu$	5299	1	283	1	808	1	2	1	1278	,	185	,	235	,	12231	1	5587	1	243	1	1199	1	0	

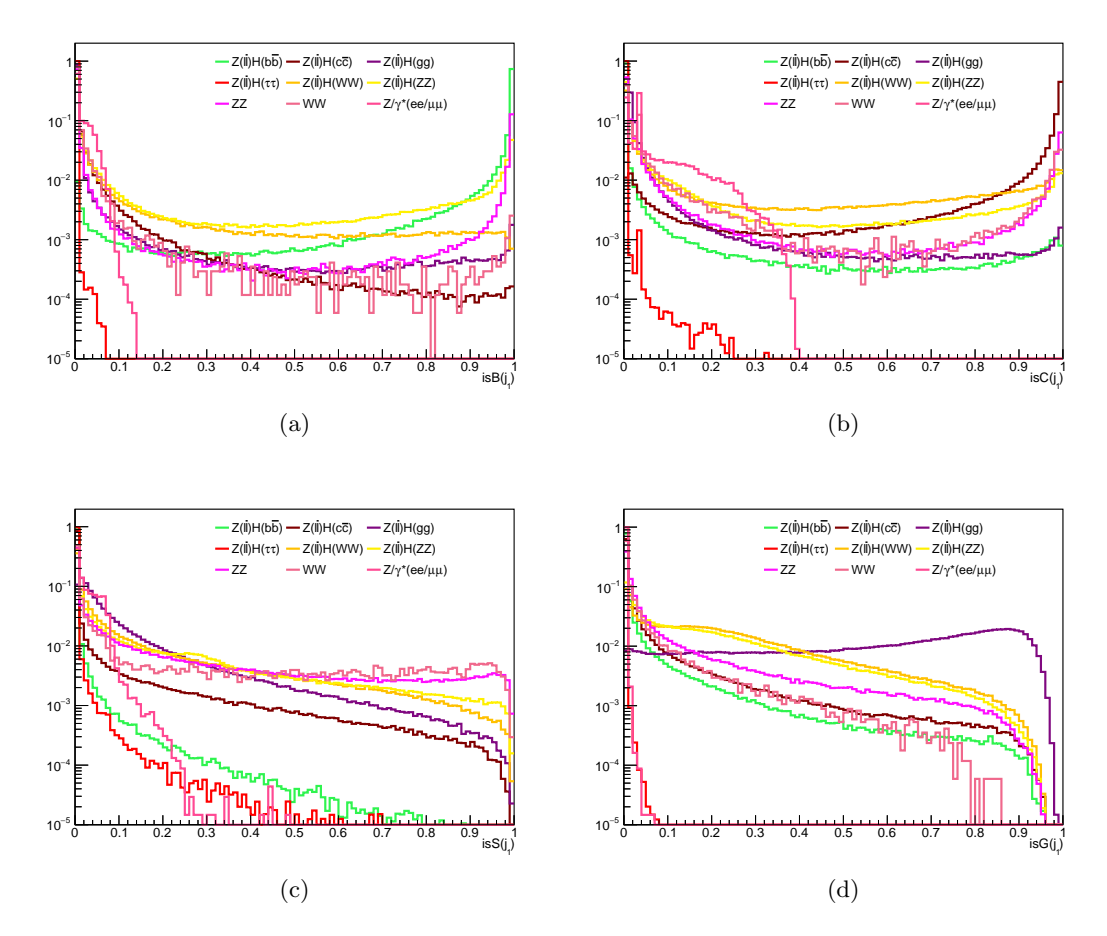


Figure 9: Distributions (normalised to unit area) in $\ell\ell H$ simulated events for selected input variables used in the neural network classification algorithm in the $\ell\ell jj$ analysis, namely the b, c, s and g tagging scores for the leading jet.

colleague Louis Portales for generating several Monte Carlo samples used in these analyses.

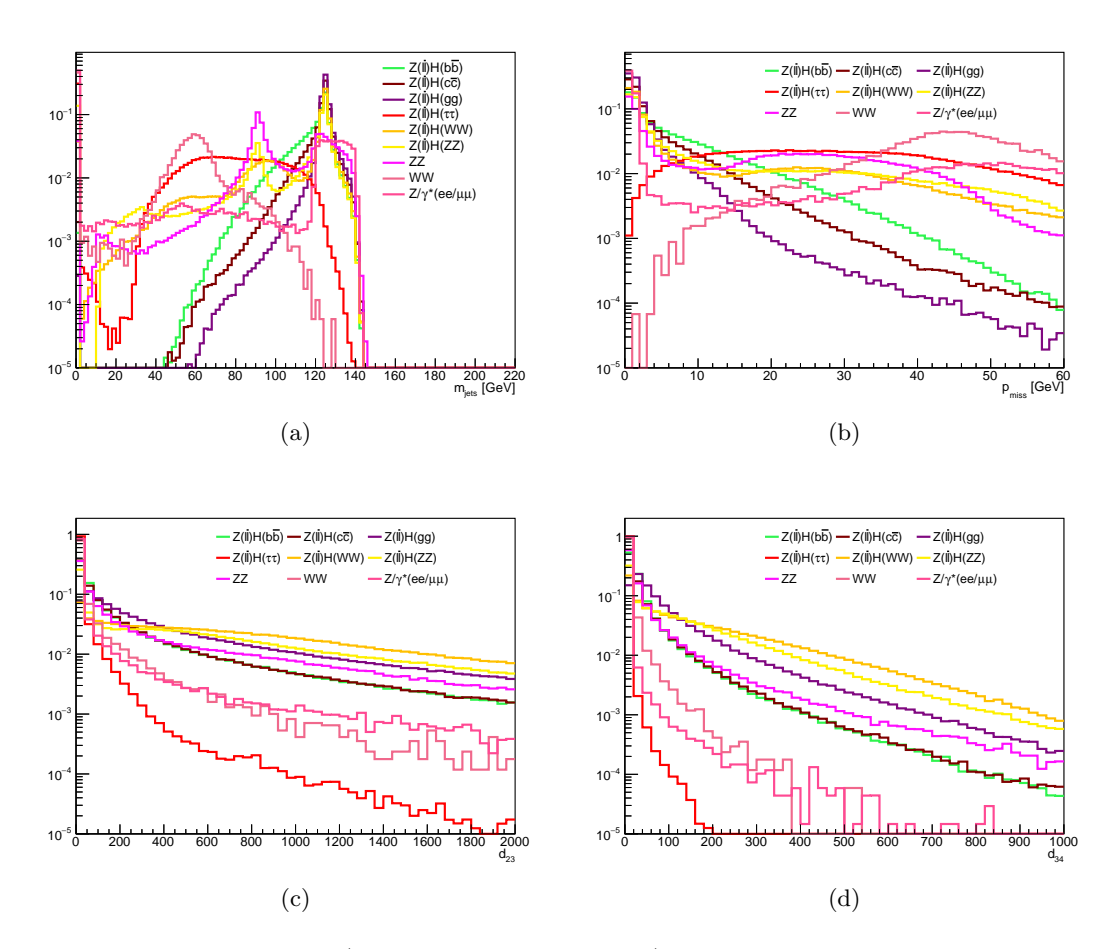


Figure 10: Distributions (normalised to unit area) in $\ell\ell H$ simulated events for selected input variables used in the neural network classification algorithm in the $\ell\ell jj$ analysis, namely the di-jet invariant mass, the missing momentum, and the jet clustering distance variables d_{23} and d_{34} .

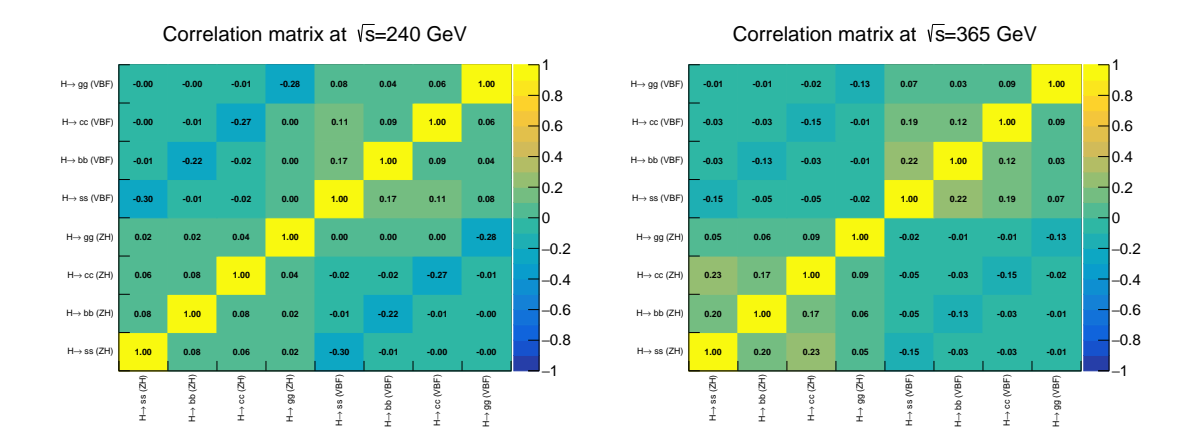


Figure 11: Correlation matrix of the combined fit for $\sqrt{s}=240\,\mathrm{GeV}$ (left) and $\sqrt{s}=365\,\mathrm{GeV}$ (right).

Table 7: Yields after each step of the selection and final efficiency for the $\nu \bar{\nu} jj$ analysis at $\sqrt{s}=365$ GeV.

	Yield	Yield	Yield after	Yield after	Efficiency (%)
Process	before selection	after lepton veto	$ \cos\theta_{\rm inv} < 0.85$	kinematics & d_{ij}	
$\nu_e \bar{\nu}_e H(gg)$	7.46×10^{3}	7.46×10^{3}	7.43×10^{3}	5.47×10^{3}	73.3
$\nu_e \bar{\nu}_e H(s\bar{s})$	2.18×10^{1}	2.18×10^{1}	2.18×10^{1}	1.60×10^{1}	73.5
$\nu_e \bar{\nu}_e H(c\bar{c})$	2.63×10^{3}	2.63×10^{3}	2.54×10^{3}	1.81×10^{3}	68.7
$ u_e \bar{\nu}_e H(b\bar{b})$	5.92×10^4	5.92×10^{4}	5.30×10^{4}	3.52×10^{4}	59.5
$\nu_e \bar{\nu}_e H(au au)$	4.99×10^{3}	4.99×10^{3}	3.52×10^{3}	6.44×10^{2}	12.9
$\nu_e \bar{\nu}_e H(ZZ)$	2.28×10^{3}	2.28×10^{3}	1.98×10^{3}	9.66×10^{2}	42.4
$\nu_e \bar{\nu}_e H(WW)$	2.11×10^{4}	2.11×10^{4}	1.48×10^{4}	8.49×10^{3}	40.1
ZH, H(gg)	6.33×10^{3}	6.33×10^{3}	6.30×10^{3}	5.46×10^{3}	86.3
$ZH,H(s\bar{s})$	1.86×10^{1}	1.86×10^{1}	1.85×10^{1}	1.61×10^{1}	86.6
$ZH,H(c\bar{c})$	2.23×10^{3}	2.23×10^{3}	2.12×10^{3}	1.83×10^{3}	82.0
$ZH, H(b\bar{b})$	4.50×10^{4}	4.50×10^{4}	3.84×10^{4}	3.30×10^{4}	73.3
$ZH, H(\tau\tau)$	4.26×10^{3}	4.26×10^{3}	2.90×10^{3}	1.40×10^{3}	32.8
ZH, H(ZZ)	1.93×10^{3}	1.93×10^{3}	1.65×10^{3}	1.12×10^{3}	58.1
ZH, H(WW)	1.61×10^{4}	1.61×10^{4}	1.11×10^{4}	8.49×10^{3}	52.7
qqH	1.03×10^{5}	1.03×10^{5}	8.20×10^{4}	9.69×10^{2}	0.94
$Z/\gamma^* \to q\bar{q}$	2.69×10^{7}	2.69×10^{7}	2.68×10^{7}	2.75×10^{3}	0.0
WW	3.26×10^{7}	3.26×10^{7}	1.99×10^7	7.29×10^{5}	2.2
ZZ	1.91×10^{6}	1.91×10^{6}	1.44×10^{6}	2.15×10^{5}	11
$tar{t}$	2.50×10^{6}	2.50×10^{6}	1.36×10^{6}	1.54×10^{4}	0.62

Table 8: Expected event yields and efficiencies (in %) for signal and background processes, after each step of the jjjj event selection, assuming an integrated luminosity $\mathcal{L}=3.12~\mathrm{ab}^{-1}$ of e^+e^- collisions at $\sqrt{s}=365~\mathrm{GeV}$. Here, $Z(q\bar{q})$ in ZH processes denotes Z boson decays to $u\bar{u}$ and $d\bar{d}$.

	Yield	Yield	Yield after	Yield after	Yield after	
Process	before	after	$m_{\rm vis}, \theta_{\rm vis}$	$d_{ m ij}$	χ^2	efficiency (%
	selection	lepton veto	requirement	requirement	requirement	
$e^+e^- \to Z(c\bar{c})H(gg)$	2.74×10^{3}	2.61×10^{3}	2.07×10^{3}	2.05×10^{3}	1.98×10^{3}	72.3
$e^+e^- \to Z(c\bar{c})H(s\bar{s})$	6.70×10^{0}	6.40×10^{0}	5.09×10^{0}	5.04×10^{0}	4.89×10^{0}	73.0
$e^+e^- \to Z(c\bar{c})H(c\bar{c})$	9.68×10^{2}	8.75×10^2	7.17×10^2	7.11×10^2	6.79×10^2	70.1
$e^+e^- \to Z(c\bar{c})H(b\bar{b})$	1.95×10^{4}	1.58×10^4	1.34×10^4	1.33×10^4	1.23×10^4	63.1
$e^+e^- \to Z(q\bar{q})H(gg)$	6.27×10^{3}	6.22×10^3	4.70×10^3	4.65×10^3	4.57×10^3	72.9
$e^+e^- \to Z(q\bar{q})H(s\bar{s})$	1.53×10^{1}	1.53×10^{1}	1.16×10^{1}	1.15×10^{1}	1.13×10^{1}	73.9
$e^+e^- \to Z(q\bar{q})H(c\bar{c})$	2.21×10^{3}	2.09×10^3	1.66×10^3	1.64×10^3	1.59×10^3	72.0
$e^+e^- \to Z(q\bar{q})H(b\bar{b})$	4.46×10^{4}	3.79×10^{4}	3.14×10^4	3.12×10^4	2.93×10^{4}	65.7
$e^+e^- \to Z(b\bar{b})H(gg)$	3.49×10^{3}	3.02×10^3	2.51×10^3	2.49×10^3	2.34×10^3	67.0
$e^+e^- \to Z(b\bar{b})H(s\bar{s})$	8.53×10^{0}	7.44×10^{0}	6.18×10^{0}	6.14×10^{0}	5.77×10^{0}	67.7
$e^+e^- \to Z(b\bar{b})H(c\bar{c})$	1.23×10^{3}	1.01×10^{3}	8.55×10^{2}	8.50×10^{2}	7.90×10^{2}	64.2
$e^+e^- \to Z(b\bar{b})H(b\bar{b})$	2.48×10^{4}	1.80×10^{4}	1.57×10^4	1.56×10^4	1.41×10^{4}	56.9
$e^+e^- \to Z(s\bar{s})H(gg)$	3.52×10^{3}	3.50×10^{3}	2.67×10^{3}	2.64×10^{3}	2.59×10^{3}	73.6
$e^+e^- \to Z(s\bar{s})H(s\bar{s})$	8.60×10^{0}	8.59×10^{0}	6.58×10^{0}	6.49×10^{0}	6.40×10^{0}	74.4
$e^+e^- \to Z(s\bar{s})H(c\bar{c})$	1.24×10^{3}	1.18×10^{3}	9.37×10^{2}	9.28×10^{2}	8.98×10^{2}	72.4
$e^+e^- \to Z(s\bar{s})H(b\bar{b})$	2.51×10^{4}	2.13×10^4	1.78×10^{4}	1.76×10^4	1.65×10^{4}	65.7
$e^+e^- \to Z(b\bar{b})H(\tau\tau)$	2.67×10^{3}	1.48×10^{3}	1.32×10^{3}	1.14×10^3	5.23×10^2	19.6
$e^+e^- \to Z(c\bar{c})H(\tau\tau)$	2.10×10^{3}	1.28×10^{3}	1.17×10^{3}	9.96×10^{2}	4.69×10^{2}	22.4
$e^+e^- \to Z(s\bar{s})H(\tau\tau)$	2.70×10^{3}	1.72×10^3	1.58×10^3	1.35×10^3	6.37×10^2	23.6
$e^+e^- \to Z(q\bar{q})H(\tau\tau)$	4.80×10^{3}	3.06×10^{3}	2.81×10^{3}	2.40×10^{3}	1.13×10^{3}	23.5
$e^+e^- \to Z(b\bar{b})H(Z\gamma)$	6.54×10^{1}	5.13×10^{1}	4.08×10^{1}	3.59×10^{1}	3.06×10^{1}	46.8
$e^+e^- \to Z(c\bar{c})H(Z\gamma)$	2.82×10^{2}	2.44×10^{2}	1.90×10^{2}	1.65×10^{2}	1.43×10^{2}	50.7
$e^+e^- \to Z(s\bar{s})H(Z\gamma)$	6.59×10^{1}	5.95×10^{1}	4.56×10^{1}	3.91×10^{1}	3.43×10^{1}	52.1
$e^+e^- \to Z(q\bar{q})H(Z\gamma)$	1.17×10^{2}	1.06×10^2	8.05×10^1	6.91×10^1	6.05×10^{1}	51.7
$e^+e^- \to Z(b\bar{b})H(WW)$	9.18×10^{3}	5.31×10^{3}	4.57×10^{3}	4.42×10^{3}	3.36×10^{3}	36.6
$e^+e^- \rightarrow Z(c\bar{c})H(WW)$	7.21×10^{3}	4.60×10^3	3.87×10^3	3.72×10^3	2.89×10^3	40.1
$e^+e^- \to Z(s\bar{s})H(WW)$	9.25×10^{3}	6.18×10^{3}	5.09×10^{3}	4.87×10^{3}	3.82×10^{3}	41.3
$e^+e^- \to Z(q\bar{q})H(WW)$	1.65×10^{4}	1.10×10^4	8.99×10^{3}	8.61×10^3	6.73×10^{3}	40.8
$e^+e^- \to Z(b\bar{b})H(ZZ)$	1.13×10^{3}	8.23×10^2	6.70×10^2	6.06×10^2	4.46×10^2	39.5
$e^+e^- \to Z(c\bar{c})H(ZZ)$	8.85×10^{2}	7.15×10^2	5.77×10^2	5.18×10^2	3.87×10^2	43.7
$e^+e^- \to Z(s\bar{s})H(ZZ)$	1.14×10^{3}	9.62×10^2	7.68×10^2	6.86×10^2	5.16×10^2	45.3
$e^+e^- \to Z(q\bar{q})H(ZZ)$	2.02×10^{3}	1.71×10^3	1.36×10^3	1.21×10^3	9.09×10^2	45.0
$e^+e^- \to \nu\bar{\nu}H$	1.18×10^{5}	9.98×10^4	2.16×10^3	9.23×10^2	0.0	0.0
$e^+e^- \to W^+W^-$	2.29×10^{7}	1.46×10^{7}	9.58×10^6	7.14×10^6	6.39×10^{6}	27.9
$e^+e^- \to ZZ$	1.38×10^{6}	1.06×10^6	5.20×10^{5}	4.52×10^{5}	4.13×10^5	29.9
$e^+e^- o Zq\bar{q}$	4.91×10^{7}	4.89×10^7	1.53×10^7	7.81×10^{6}	7.57×10^6	15.4
$e^+e^- \to t\bar{t}$	1.86×10^{6}	9.94×10^{5}	9.38×10^{5}	9.18×10^{5}	7.04×10^{5}	37.8

References

- [1] ATLAS Collaboration, Observation of a new particle in the search for the Standard Model Higgs boson with the ATLAS detector at the LHC, Phys. Lett. B 716 (2012) 1 [1207.7214].
- [2] CMS Collaboration, Observation of a new boson at a mass of 125 GeV with the CMS experiment at the LHC, Phys. Lett. B 716 (2012) 30 [1207.7235].
- [3] ATLAS Collaboration, A detailed map of Higgs boson interactions by the ATLAS experiment ten years after the discovery, Nature 607 (2022) 52 [2207.00092].
- [4] CMS Collaboration, A portrait of the Higgs boson by the CMS experiment ten years after the discovery, Nature 607 (2022) 60 [2207.00043].
- [5] ATLAS Collaboration, Observation of $H \to b\bar{b}$ decays and VH production with the ATLAS detector, Phys. Lett. B **786** (2018) 59 [1808.08238].
- [6] CMS Collaboration, Observation of Higgs Boson Decay to Bottom Quarks, Phys. Rev. Lett. 121 (2018) 121801 [1808.08242].
- [7] ATLAS Collaboration, Cross-section measurements of the Higgs boson decaying into a pair of τ -leptons in proton-proton collisions at $\sqrt{s} = 13$ TeV with the ATLAS detector, Phys. Rev. D 99 (2019) 072001 [1811.08856].
- [8] CMS Collaboration, Observation of the Higgs boson decay to a pair of τ leptons with the CMS detector, Phys. Lett. B 779 (2018) 283 [1708.00373].
- [9] ATLAS Collaboration, Observation of Higgs boson production in association with a top quark pair at the LHC with the ATLAS detector, Phys. Lett. B 784 (2018) 173 [1806.00425].
- [10] CMS Collaboration, Observation of $t\bar{t}H$ Production, Phys. Rev. Lett. 120 (2018) 231801 [1804.02610].
- [11] ATLAS Collaboration, Evidence for the dimuon decay of the Higgs boson in pp collisions with the ATLAS detector, 2507.03595.
- [12] CMS Collaboration, Evidence for Higgs boson decay to a pair of muons, JHEP **01** (2021) 148 [2009.04363].
- [13] ATLAS and CMS Collaborations, Evidence for the Higgs Boson Decay to a Z Boson and a Photon at the LHC, Phys. Rev. Lett. 132 (2024) 021803 [2309.03501].
- [14] F. Englert and R. Brout, Broken Symmetry and the Mass of Gauge Vector Mesons, Phys. Rev. Lett. 13 (1964) 321.
- [15] P.W. Higgs, Broken symmetries, massless particles and gauge fields, Phys. Lett. 12 (1964) 132.
- [16] M. Cepeda et al., Report from Working Group 2: Higgs Physics at the HL-LHC and HE-LHC, CERN Yellow Rep. Monogr. 7 (2019) 221 [1902.00134].
- [17] M.E. Peskin, Model-Agnostic Exploration of the Mass Reach of Precision Higgs Boson Coupling Measurements, in Snowmass 2021, 9, 2022 [2209.03303].
- [18] ATLAS AND CMS collaboration, Highlights of the HL-LHC physics projections by ATLAS and CMS, 2504.00672.
- [19] Particle Data Group collaboration, Review of particle physics, Phys. Rev. D 110 (2024) 030001.

- [20] FCC collaboration, FCC-ee: The Lepton Collider: Future Circular Collider Conceptual Design Report Volume 2, Eur. Phys. J. ST 228 (2019) 261.
- [21] FCC collaboration, Future Circular Collider Feasibility Study Report: Volume 1, Physics, Experiments, Detectors, 2505.00272.
- [22] LINEAR COLLIDER VISION collaboration, A Linear Collider Vision for the Future of Particle Physics, 2503.19983.
- [23] IDEA STUDY GROUP collaboration, The IDEA detector concept for FCC-ee, 2502.21223.
- [24] J. Eysermans, G. Bernardi and L. Ang, Higgs boson mass and model-independent zh crosssection at fcc-ee in the di-electron and di-muon final states, Mar., 2025. 10.17181/jfb44-s0d81.
- [25] M. Selvaggi, J. Eysermans and A. Blondel, *Prospects in electroweak, higgs and top physics at fcc*, Mar., 2025. 10.17181/n78xk-qcv56.
- [26] J. de Blas et al., Physics Briefing Book: Input for the 2026 update of the European Strategy for Particle Physics, 2511.03883.
- [27] The IDEA Study Group, The IDEA detector concept for FCC-ee, 2502.21223.
- [28] W. Kilian, T. Ohl and J. Reuter, WHIZARD: Simulating Multi-Particle Processes at LHC and ILC, Eur. Phys. J. C 71 (2011) 1742 [0708.4233].
- [29] T. Sjostrand, S. Mrenna and P.Z. Skands, PYTHIA 6.4 Physics and Manual, JHEP 05 (2006) 026 [hep-ph/0603175].
- [30] T. Sjöstrand, S. Ask, J.R. Christiansen, R. Corke, N. Desai, P. Ilten et al., An introduction to PYTHIA 8.2, Comput. Phys. Commun. 191 (2015) 159 [1410.3012].
- [31] DELPHES 3 collaboration, DELPHES 3, A modular framework for fast simulation of a generic collider experiment, JHEP 02 (2014) 057 [1307.6346].
- [32] M. Selvaggi, DELPHES 3: A modular framework for fast-simulation of generic collider experiments, J. Phys. Conf. Ser. **523** (2014) 012033.
- [33] M. Selvaggi, Delphes 3: Latest Developments, J. Phys. Conf. Ser. 762 (2016) 012051.
- [34] F. Bedeschi, L. Gouskos and M. Selvaggi, Jet flavour tagging for future colliders with fast simulation, Eur. Phys. J. C 82 (2022) 646 [2202.03285].
- [35] S. Catani, Y.L. Dokshitzer, M. Olsson, G. Turnock and B.R. Webber, New clustering algorithm for multi-jet cross-sections in e⁺e⁻ annihilation, Phys. Lett. B **269** (1991) 432.
- [36] M. Cacciari, G.P. Salam and G. Soyez, FastJet user manual, Eur. Phys. J. C 72 (2012) 1896 [1111.6097].
- [37] S. Aumiller, D. Garcia and M. Selvaggi, Jet-Flavor Tagging Performance at FCC-ee, 2024. 10.17181/8g834-jv464.
- [38] F. Chollet, Keras, https://github.com/fchollet/keras (2015) .
- [39] M. Abadi, A. Agarwal, P. Barham, E. Brevdo, Z. Chen, C. Citro et al., *TensorFlow: Large-scale machine learning on heterogeneous systems*, 2015.
- [40] V.D. Barger, K.-m. Cheung, A. Djouadi, B.A. Kniehl and P.M. Zerwas, *Higgs bosons:*Intermediate mass range at e+ e- colliders, *Phys. Rev. D* 49 (1994) 79 [hep-ph/9306270].

[41] R.J. Barlow and C. Beeston, Fitting using finite Monte Carlo samples, Comput. Phys. Commun. 77 (1993) 219.